F. Cavenago, A.M. Giordano, M. Massari
Contact Detection, Isolation and Estimation for Orbital Robots Through an Observer Based on a Centroid-Joints Dynamics
Acta Astronautica, Vol. 181, 2021, p. 40-51
doi:10.1016/j.actaastro.2021.01.001

Contact detection, isolation and estimation for orbital robots through an observer based on a centroid-joints dynamics

Francesco Cavenago[a,*], Alessandro M. Giordano[b], Mauro Massari[a]

[a] *Department of Aerospace Science and Technology, Politecnico di Milano, via La Masa 34, 20156, Milano, Italy*
[b] *DLR Institute of Robotics and Mechatronics, 82234, Weßling, Germany*

Abstract

In this paper, the contact force detection, isolation and estimation problems for an orbital robot are addressed. First, an observer based on a base-joints dynamics is reviewed and analyzed considering the issues related to a space robotic application. Then, a new scheme is derived reformulating the dynamics in terms of the motion of the centroid of the whole robot and the joints. In both observers, three momentum-based residuals are defined, which can be used to reconstruct the external contact wrench. The reconstruction through the proposed observer turns out to provide superior performance with respect to the base-joints one thanks to the decoupling of the angular and joint momentum residuals from the spacecraft linear velocity, which is an inaccurate measurement in real space scenarios. The advantages of the proposed observer are shown through both simulative and hardware validation featuring a 7 degrees of freedom (DoF) arm mounted on a 6 DoF moving base.

Keywords: Contact force estimation; Floating-base space robots; Nonlinear observer; Collision detection and isolation

1. Introduction

Orbital robotics is considered one of the key technologies for many future missions since it can provide higher levels of safety, reliability and performance [1]. Especially, space manipulators are considered one of the most promising technology for servicing, assembly and inspection in orbit. However, their use is still very limited due to the high complexity involved. One of the most challenging issue is dealing with physical contact between the robot and a target object.

Since the beginning, the dynamics of the contact phase has been extensively studied, considering free-floating robots [2][3][4][5]. Many authors have addressed the problem of guaranteeing a safe interaction when the robot's end-effector comes into contact with the target to perform grasping tasks [6][7][8][9][10]. In this context, effective control strategies can take advantage of the accurate knowledge of the contact force, which can be measured by employing a force-torque sensor (FTS) duly placed at the wrist. However, a strategy relying only on this sensor is not robust since a failure in the FTS could compromise the correct completion of the task, or even block the operations until repair. Furthermore, the FTS measures forces and torques acting only at the end-effector, and thus contacts that do not occur exactly there, e.g. a contact on links

*Corresponding author
Email address: francesco.cavenago@polimi.it (Francesco Cavenago)

other than the one with the FTS, cannot be measured.

These motivations have pushed some researchers to propose a different approach, in which the contact force is estimated without using a dedicated sensor. In [11] the use of the disturbance observer is proposed, while in [6] the force is estimated through the target's equations of motion. Both methods require quantities that are not measured directly, i.e., the joint accelerations, the linear velocity and the angular acceleration of the robot base for the former, and the target's accelerations for the latter. These quantities could be obtained through numerical differentiation, but they would introduce nonnegligible noise in the estimation process. Moreover, these methods assume to know where the force acts, i.e. at the end-effector, and thus cannot be used for a more general situation of a contact on a generic link.

The problem of estimating a contact force involving whichever part of the robot has been extensively studied within the robotics community in the last years, especially for fixed-base robots [12][13][14], humanoids [15][16], and flying robots [17]. On the other hand, few works have been carried out considering orbital robots. In [15] the well-known generalized momemtum-based observer, originally presented in [12] for fixed-base robots, is extended to humanoids, featuring a floating-base dynamics similar to the one of space robots. This observer computes linear, angular and joint momentum residuals which turn out to be the estimates of the external generalized forces acting on the floating base and the disturbance joint torques due to a contact. Then, the residuals can be used to estimate the external wrench acting on the robot. The main drawback of the method is the need of a fast and accurate reconstruction of the base linear velocity, which is difficult to obtain in the the case of a real space application.

In this paper, the residual-based observer [15] is reviewed and analyzed considering the issues related to a space robot. Then, a new observer is derived, which is based on a centroid-joints dynamics. The most important feature of the new observer is the complete decoupling from the base linear velocity of the angular and joints momentum residuals, which, therefore, result to be less noisy. This leads to a better-performing estimation of the contact wrench than [15]. Indeed, the wrench reconstruction can be performed using only these two residuals, and thus not requiring a measurement of the base linear velocity, but measuring solely the angular velocity, and the joint positions, velocities and torques, which can be acquired at high frequency and feature relatively low noise.

Furthermore, the proposed method allows reconstructing a contact on a generic point, and not only at the end-effector. It can be used to detect, locate and estimate unexpected collisions which may occur during the robot's operations. The proposed strategy to isolate the collision uses only the information from the angular and joint momentum residuals of the presented observer. Consequently, the contact point can be found relying only on accurate sensors working at high frequency, and thus an accurate and fast wrench estimation is achieved.

The main contributions of this paper are: 1) the formulation of the observer [15] for application on an actuated space robot, the analysis of its limitations, and the development of a new observer based on a centroid-joints dynamics which solves these limitations; 2) a new method to identify a generic contact point along the robot, using only the angular and joint momentum residuals; 3) the experimental validation of both observers on the On-Orbit Servicing Simulator (OOS-Sim) hardware-in-the-loop facility [18] at the DLR. Note that, to the best of the authors' knowledge, no experimental tests have been performed for the observer [15] before. The work in this paper is an extension of the authors' preliminary analyses presented in [19].

The paper is structured as follows: in Sect. 2, the notation, the assumptions and the equations are introduced. In Sect. 3, the method in [15] is formulated for space robots and the proposed observer based on a centroid-joints dynamics is presented. In Sect. 4, the reconstruction of the external wrench is addressed. In Sect. 5, a strategy to isolate the generic contact point is presented. In Sect. 6, a simulation example is proposed to compare the performance of the observers. In Sect. 7, the results of the experimental validation of the observers are reported. Finally, in Sect. 8, the main conclusions are drawn and future works are discussed.

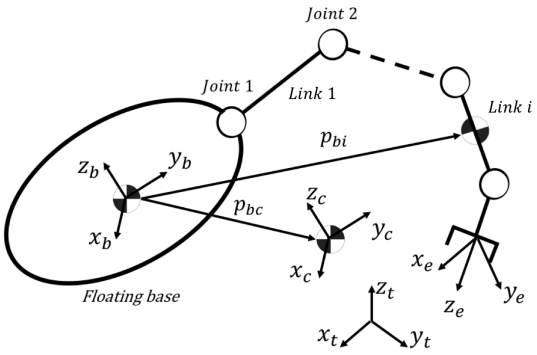

Figure 1: Floating space robot.

2. Preliminaries

2.1. Problem statement and assumptions

A space robot is considered as a multibody system composed of $n+1$ rigid bodies connected with n revolute joints (see Fig. 1). An in-orbit proximity operation is taken as reference scenario. The robot is required to perform manipulation or inspection tasks, and thus to operate close to one or more other objects. In this context, contact situations may arise and they can be planned, e.g. grasping a target, or unexpected, e.g. a collision. In the former case, the accurate knowledge of the contact force at the end-effector is important to guarantee a safe interaction, while, in the latter case, the force estimate can be used to detect and isolate the collision and to implement a safe reaction. In this study, no disturbances caused by the environment (e.g. gravity gradient, solar pressure, air drag and magnetic forces) are taken into account, because they are considerably smaller than the actuation forces. Note that this is a commonly accepted assumption in space robotics. Finally, a contact on a generic point along the robot is considered. This situation is very general, including both planned contact at the end-effector and unexpected collision.

2.2. Main notations

Four main reference frames are defined. One, denoted by $\mathcal{B}$, is the body frame located on the center-of-mass (CM) of the spacecraft. The second one, denoted by $\mathcal{C}$, is a frame with rotating axes, always parallel to $\mathcal{B}$, placed on the CM of the space robot. The third one, denoted by $\mathcal{E}$, is a frame located on the end-effector. The last one is the inertial frame, denoted by $\mathcal{T}$.

In order to transform forces and velocities between reference frames, the Adjoint transformation [20] is introduced:

$$\boldsymbol{A}_{xy} = \begin{bmatrix} \boldsymbol{R}_{xy} & [\boldsymbol{p}_{xy}]^{\wedge}\boldsymbol{R}_{xy} \\ \boldsymbol{0} & \boldsymbol{R}_{xy} \end{bmatrix} \in \mathbb{R}^{6\times 6}, \tag{1}$$

where $\boldsymbol{p}_{xy} \in \mathbb{R}^3$ and $\boldsymbol{R}_{xy} \in \mathrm{SO}(3)$ indicate the generic position vector, expressed in $\mathcal{X}$, and rotation matrix from frame $\mathcal{X}$ to frame $\mathcal{Y}$, respectively. The operator $[\cdot]^{\wedge}$ stands for the skew-symmetric matrix of the

argument. Finally, the identity matrix and zero matrix are denoted by $\boldsymbol{E}$ and $\boldsymbol{0}$ of suitable dimensions, respectively.

2.3. Dynamics of the impact phase

The dynamics of the space robot can be expressed as follows:

$$\underbrace{\begin{bmatrix} \boldsymbol{M}_t & \boldsymbol{M}_{tr} & \boldsymbol{M}_{tm} \\ \boldsymbol{M}_{tr}^T & \boldsymbol{M}_r & \boldsymbol{M}_{rm} \\ \boldsymbol{M}_{tm}^T & \boldsymbol{M}_{rm}^T & \boldsymbol{M}_m \end{bmatrix}}_{\boldsymbol{M}(\boldsymbol{q})} \begin{bmatrix} \dot{\boldsymbol{v}}_b \\ \dot{\boldsymbol{\omega}}_b \\ \ddot{\boldsymbol{q}} \end{bmatrix} + \underbrace{\begin{bmatrix} \boldsymbol{C}_t & \boldsymbol{C}_{tr} & \boldsymbol{C}_{tm} \\ \boldsymbol{C}_{rt} & \boldsymbol{C}_r & \boldsymbol{C}_{rm} \\ \boldsymbol{C}_{mt} & \boldsymbol{C}_{mr} & \boldsymbol{C}_m \end{bmatrix}}_{\boldsymbol{C}(\boldsymbol{q},\dot{\boldsymbol{q}},\boldsymbol{v}_b,\boldsymbol{\omega}_b)} \begin{bmatrix} \boldsymbol{v}_b \\ \boldsymbol{\omega}_b \\ \dot{\boldsymbol{q}} \end{bmatrix} = \begin{bmatrix} \boldsymbol{f}_b \\ \boldsymbol{m}_b \\ \boldsymbol{\tau} \end{bmatrix} + \begin{bmatrix} \boldsymbol{f}_{ext,b} \\ \boldsymbol{m}_{ext,b} \\ \boldsymbol{\tau}_{ext} \end{bmatrix}, \tag{2}$$

where

$$\begin{bmatrix} \boldsymbol{f}_{ext,b} \\ \boldsymbol{m}_{ext,b} \\ \boldsymbol{\tau}_{ext} \end{bmatrix} = \begin{bmatrix} \boldsymbol{A}_{pb}^T \\ \boldsymbol{J}_p^T \end{bmatrix} \boldsymbol{\mathcal{F}}_{ext}, \tag{3}$$

and where $\boldsymbol{\mathcal{F}}_{ext} = [\boldsymbol{f}_{ext}^T \ \boldsymbol{m}_{ext}^T]^T \in \mathbb{R}^6$ is the contact wrench at a generic point p along the robot; $\boldsymbol{f}_{ext,b}, \boldsymbol{m}_{ext,b} \in \mathbb{R}^3$ are the force and moment acting at base level due to the external contact; $\boldsymbol{\tau}_{ext} \in \mathbb{R}^n$ is the vector of the external joint torques due to the contact; $\boldsymbol{J}_p = [\boldsymbol{J}_{vp}^T \ \boldsymbol{J}_{\omega p}^T]^T \in \mathbb{R}^{6\times n}$ is the fixed-base robot's Jacobian for the point p, with $\boldsymbol{J}_{vp} \in \mathbb{R}^{3\times n}$, $\boldsymbol{J}_{\omega p} \in \mathbb{R}^{3\times n}$ being the Jacobians mapping $\dot{\boldsymbol{q}}$ into the linear and angular velocity of a frame on the contact point p, respectively; $\boldsymbol{v}_b, \boldsymbol{\omega}_b \in \mathbb{R}^3$ are the linear and angular velocity of the base expressed in $\mathcal{B}$; $\boldsymbol{q}, \dot{\boldsymbol{q}} \in \mathbb{R}^n$ are the joint angles and velocities; $\boldsymbol{f}_b, \boldsymbol{m}_b \in \mathbb{R}^3$ are the commanded base force and moment around $\mathcal{B}$, expressed in $\mathcal{B}$; $\boldsymbol{\tau} \in \mathbb{R}^n$ are the commanded joint torques; the submatrices $\boldsymbol{M}_t, \boldsymbol{M}_{tr}, \boldsymbol{M}_r \in \mathbb{R}^{3\times 3}$ compose the inertia matrix of the composite rigid body; the submatrices $\boldsymbol{M}_{tm}, \boldsymbol{M}_{rm} \in \mathbb{R}^{3\times n}$ are the coupling inertia matrices; $\boldsymbol{M}_m \in \mathbb{R}^{n\times n}$ is the inertia matrix of the manipulator; $\boldsymbol{C}(\boldsymbol{q}, \dot{\boldsymbol{q}}, \boldsymbol{v}_b, \boldsymbol{\omega}_b) \in \mathbb{R}^{(6+n)\times(6+n)}$ is the Coriolis/centrifugal matrix. The analytical expressions of the inertia matrix can be found in [21].

The total generalized momentum around $\mathcal{B}$ and expressed in $\mathcal{B}$, denoted by $\boldsymbol{h}_b \in \mathbb{R}^6$, results in

$$\boldsymbol{h}_b = \begin{bmatrix} \boldsymbol{h}_b^t \\ \boldsymbol{h}_b^r \end{bmatrix} = \begin{bmatrix} \boldsymbol{M}_t & \boldsymbol{M}_{tr} \\ \boldsymbol{M}_{tr}^T & \boldsymbol{M}_r \end{bmatrix} \begin{bmatrix} \boldsymbol{v}_b \\ \boldsymbol{\omega}_b \end{bmatrix} + \begin{bmatrix} \boldsymbol{M}_{tm} \\ \boldsymbol{M}_{rm} \end{bmatrix} \dot{\boldsymbol{q}}, \tag{4}$$

with $\boldsymbol{h}_b^t, \boldsymbol{h}_b^r \in \mathbb{R}^3$ being the translational and rotational momentum, respectively.

3. Nonlinear force observer for space robots

In this section, the residual-based observer presented in [15] for humanoids is firstly adapted to space robots. This method is based on the momentum-based observer [13] in which a residual vector is defined as the difference between the generalized momentum of the fixed-base robot and its estimate. Under ideal condition, this residual vector turns out to be a filtered estimation of the external disturbance on the joints. Hereafter, the same idea is followed using the dynamics model (2) to obtain estimates of $\boldsymbol{f}_{ext,b}$, $\boldsymbol{m}_{ext,b}$ and $\boldsymbol{\tau}_{ext}$. Afterwards, the proposed observer, based on a centroid-joints dynamics, is derived and discussed. Interesting decoupling properties from the linear velocity of the base are highlighted, which allow improving the performance when real implementation issues are considered.

3.1. Observer based on a base-joints dynamics

Considering Eq. (2), the dynamics of the robot can be split into base translational and rotational dynamics, i.e., the first and second rows of the equation, and joint dynamics, i.e., the third row of the equation. Denoting by $\hat{\boldsymbol{f}}_{ext,b}, \hat{\boldsymbol{m}}_{ext,b} \in \mathbb{R}^3$ and $\hat{\boldsymbol{\tau}}_{ext} \in \mathbb{R}^n$ the residuals, they are designed as follows:

$$\hat{\boldsymbol{f}}_{ext,b} = \boldsymbol{K}_f(\underbrace{\boldsymbol{M}_t\boldsymbol{v}_b + \boldsymbol{M}_{tr}\boldsymbol{\omega}_b + \boldsymbol{M}_{tm}\dot{\boldsymbol{q}}}_{\boldsymbol{h}_b^t} - \int_0^t (\boldsymbol{f}_b + \boldsymbol{C}_t^T\boldsymbol{v}_b + \boldsymbol{C}_{rt}^T\boldsymbol{\omega}_b + \boldsymbol{C}_{mt}^T\dot{\boldsymbol{q}} + \hat{\boldsymbol{f}}_{ext,b})ds), \tag{5a}$$

$$\hat{\boldsymbol{m}}_{ext,b} = \boldsymbol{K}_m(\underbrace{\boldsymbol{M}_{tr}^T\boldsymbol{v}_b + \boldsymbol{M}_r\boldsymbol{\omega}_b + \boldsymbol{M}_{rm}\dot{\boldsymbol{q}}}_{\boldsymbol{h}_b^r} - \int_0^t (\boldsymbol{m}_b + \boldsymbol{C}_{tr}^T\boldsymbol{v}_b + \boldsymbol{C}_r^T\boldsymbol{\omega}_b + \boldsymbol{C}_{mr}^T\dot{\boldsymbol{q}} + \hat{\boldsymbol{m}}_{ext,b})ds), \tag{5b}$$

$$\hat{\boldsymbol{\tau}}_{ext} = \boldsymbol{K}_\tau(\underbrace{\boldsymbol{M}_{tm}^T\boldsymbol{v}_b + \boldsymbol{M}_{rm}^T\boldsymbol{\omega}_b + \boldsymbol{M}_m\dot{\boldsymbol{q}}}_{\boldsymbol{h}_j} - \int_0^t (\boldsymbol{\tau} + \boldsymbol{C}_{tm}^T\boldsymbol{v}_b + \boldsymbol{C}_{rm}^T\boldsymbol{\omega}_b + \boldsymbol{C}_m^T\dot{\boldsymbol{q}} + \hat{\boldsymbol{\tau}}_{ext})ds), \tag{5c}$$

where $\boldsymbol{K}_f, \boldsymbol{K}_m \in \mathbb{R}^{3\times3}$, and $\boldsymbol{K}_\tau \in \mathbb{R}^{n\times n}$ are positive-definite diagonal matrices containing the observer gains; $\boldsymbol{h}_j \in \mathbb{R}^n$ is the joints generalized momentum.
By differentiating Eqs. (5a), (5b), and (5c), and by exploiting the dynamics (2) and the property $\dot{\boldsymbol{M}} = \boldsymbol{C} + \boldsymbol{C}^T$, the following equations result

$$\dot{\hat{\boldsymbol{f}}}_{ext,b} = \boldsymbol{K}_f(\boldsymbol{f}_{ext,b} - \hat{\boldsymbol{f}}_{ext,b}), \tag{6a}$$

$$\dot{\hat{\boldsymbol{m}}}_{ext,b} = \boldsymbol{K}_m(\boldsymbol{m}_{ext,b} - \hat{\boldsymbol{m}}_{ext,b}), \tag{6b}$$

$$\dot{\hat{\boldsymbol{\tau}}}_{ext} = \boldsymbol{K}_\tau(\boldsymbol{\tau}_{ext} - \hat{\boldsymbol{\tau}}_{ext}), \tag{6c}$$

which express the relation between the estimated and true quantities.
From Eq. (6) it can be noticed that $\hat{\boldsymbol{f}}_{ext,b}$, $\hat{\boldsymbol{m}}_{ext,b}$, and $\hat{\boldsymbol{\tau}}_{ext}$ are first-order-filtered estimations of $\boldsymbol{f}_{ext,b}$, $\boldsymbol{m}_{ext,b}$, and $\boldsymbol{\tau}_{ext}$, respectively.
Increasing the observer gains reduces the time constants of the transient response of the estimates, and thus leads to a faster estimation of $\boldsymbol{f}_{ext,b}, \boldsymbol{m}_{ext,b}$, and $\boldsymbol{\tau}_{ext}$. Ideally, if the observer gains tend to infinity, it would be achieved $\hat{\boldsymbol{f}}_{ext,b} \approx \boldsymbol{f}_{ext,b}$, $\hat{\boldsymbol{m}}_{ext,b} \approx \boldsymbol{m}_{ext,b}$ and $\hat{\boldsymbol{\tau}}_{ext} \approx \boldsymbol{\tau}_{ext}$, respectively. However, in practice, noise and uncertainties induce an upper bound on the values that the observer gains can take. Moreover, the computation of all the residuals, i.e., $\hat{\boldsymbol{f}}_{ext,b}$, $\hat{\boldsymbol{m}}_{ext,b}$, and $\hat{\boldsymbol{\tau}}_{ext}$, requires the knowledge of the base linear velocity $\boldsymbol{v}_b$. A fast and accurate estimation of the linear velocity is particularly difficult in practical applications and the observer scheme (5) would require very low gains resulting in limited response bandwidth. This limitation motivates the derivation of the proposed observer presented hereafter, which turns out to be more practical and better-performing.

3.2. Observer based on a centroid-joints dynamics

In this section, the robot dynamics is transformed using a new set of generalized velocities: the linear velocity of the CM of the whole system, the angular momentum around $\mathcal{C}$ expressed in $\mathcal{C}$ and the joint velocities. Afterwards, the transformed dynamics is used to formulate the new observer scheme.

Let $\boldsymbol{h}_c \in \mathbb{R}^6$ denote the total momentum around $\mathcal{C}$. It can be computed as $\boldsymbol{h}_c = \boldsymbol{A}_{cb}^{-T}\boldsymbol{h}_b$ [21][1], resulting in

$$\boldsymbol{h}_c = \begin{bmatrix} \boldsymbol{h}_c^t \\ \boldsymbol{h}_c^r \end{bmatrix} = \begin{bmatrix} m\boldsymbol{E} & -m[\boldsymbol{p}_{bc}]^\wedge & m\bar{\boldsymbol{J}}_v \\ \boldsymbol{0} & \boldsymbol{I}_c & \boldsymbol{I}_c\bar{\boldsymbol{J}}_\omega \end{bmatrix} \begin{bmatrix} \boldsymbol{v}_b \\ \boldsymbol{\omega}_b \\ \dot{\boldsymbol{q}} \end{bmatrix}, \tag{7}$$

where $\boldsymbol{h}_c^t \in \mathbb{R}^3$ is the translational momentum and $\boldsymbol{h}_c^r \in \mathbb{R}^3$ is the rotational momentum around $\mathcal{C}$, both expressed in $\mathcal{C}$, $m \in \mathbb{R}$ and $\boldsymbol{I}_c \in \mathbb{R}^{3\times3}$ are the mass and the rotational inertia around $\mathcal{C}$ of the whole body, and $\bar{\boldsymbol{J}}_v, \bar{\boldsymbol{J}}_\omega \in \mathbb{R}^{3\times n}$ are computed as follows

$$\bar{\boldsymbol{J}}_v = \frac{1}{m}\sum_{i=1}^{n} m_i \boldsymbol{R}_{ib}^T \boldsymbol{J}_{vi}, \tag{8}$$

$$\bar{\boldsymbol{J}}_\omega = \boldsymbol{I}_c^{-1}\sum_{i=1}^{n} \boldsymbol{R}_{ib}^T \boldsymbol{I}_i \boldsymbol{J}_{\omega i} + m_i[\boldsymbol{p}_{bi}]^\wedge(\boldsymbol{J}_{vi} - \bar{\boldsymbol{J}}_v), \tag{9}$$

with $m_i \in \mathbb{R}$ and $\boldsymbol{I}_i \in \mathbb{R}^{3\times3}$ being the mass and rotational inertia of body i, computed around its CM, and $\boldsymbol{J}_{vi}, \boldsymbol{J}_{\omega i} \in \mathbb{R}^{3\times n}$ being the Jacobians mapping $\dot{\boldsymbol{q}}$ in the linear and angular velocity of body i, respectively. The Jacobians $\bar{\boldsymbol{J}}_v$ and $\bar{\boldsymbol{J}}_\omega$ can be also computed based on the inertia model in (2) as:

$$\bar{\boldsymbol{J}}_v = \frac{1}{m}\boldsymbol{M}_{tm}, \tag{10}$$

$$\bar{\boldsymbol{J}}_\omega = \left(\boldsymbol{M}_r - \frac{1}{m}\boldsymbol{M}_{tr}^T\boldsymbol{M}_{tr}\right)^{-1}\left(\boldsymbol{M}_{rm} - \frac{1}{m}\boldsymbol{M}_{tr}^T\boldsymbol{M}_{tm}\right). \tag{11}$$

Introducing the linear velocity of the CM of the whole system, $\boldsymbol{v}_c = \frac{1}{m}\boldsymbol{h}_c^t \in \mathbb{R}^3$, and exploiting Eq. (7), a transformation matrix $\boldsymbol{\Gamma} \in \mathbb{R}^{(6+n)\times(6+n)}$ can be defined as

$$\begin{bmatrix} \boldsymbol{v}_c \\ \boldsymbol{h}_c^r \\ \dot{\boldsymbol{q}} \end{bmatrix} = \underbrace{\begin{bmatrix} \boldsymbol{E} & -[\boldsymbol{p}_{bc}]^\wedge & \bar{\boldsymbol{J}}_v \\ \boldsymbol{0} & \boldsymbol{I}_c & \boldsymbol{I}_c\bar{\boldsymbol{J}}_\omega \\ \boldsymbol{0} & \boldsymbol{0} & \boldsymbol{E} \end{bmatrix}}_{\boldsymbol{\Gamma}} \begin{bmatrix} \boldsymbol{v}_b \\ \boldsymbol{\omega}_b \\ \dot{\boldsymbol{q}} \end{bmatrix}. \tag{12}$$

Consequently, the generalized forces transform as

$$\begin{bmatrix} \boldsymbol{f}_b \\ \boldsymbol{m}_b \\ \boldsymbol{\tau} \end{bmatrix} = \boldsymbol{\Gamma}^T \begin{bmatrix} \boldsymbol{f}_c \\ \boldsymbol{a}_c \\ \bar{\boldsymbol{\tau}} \end{bmatrix}, \tag{13}$$

$$\begin{bmatrix} \boldsymbol{f}_{ext,b} \\ \boldsymbol{m}_{ext,b} \\ \boldsymbol{\tau}_{ext} \end{bmatrix} = \boldsymbol{\Gamma}^T \begin{bmatrix} \boldsymbol{f}_{ext,c} \\ \boldsymbol{a}_{ext,c} \\ \bar{\boldsymbol{\tau}}_{ext} \end{bmatrix}, \tag{14}$$

[1] The equations used herein are slightly different from the ones presented in [21]: in [21] the frame $\mathcal{C}$ is nonrotating, whereas here $\mathcal{C}$ is rotating, parallel to $\mathcal{B}$.

where $\boldsymbol{f}_c \in \mathbb{R}^3$, $\boldsymbol{a}_c \in \mathbb{R}^3$, and $\bar{\boldsymbol{\tau}} \in \mathbb{R}^n$ are new control inputs; $\boldsymbol{f}_{ext,c} \in \mathbb{R}^3$, $\boldsymbol{a}_{ext,c} \in \mathbb{R}^3$, and $\bar{\boldsymbol{\tau}}_{ext} \in \mathbb{R}^n$ are the projections of the external wrench $\boldsymbol{\mathcal{F}}_{ext}$ into the new variables space.
Then, the dynamics in the new states is derived by pre-multiplying (2) by $\boldsymbol{\Gamma}^{-T}$ and substituting $\boldsymbol{v}_b$, $\boldsymbol{\omega}_b$, $\dot{\boldsymbol{q}}$ and their derivatives, isolated from Eq. (12), in (2). The resulting system is

$$\begin{bmatrix} m\boldsymbol{E} & \boldsymbol{0} & \boldsymbol{0} \\ \boldsymbol{0} & \boldsymbol{I}_c^{-1} & \boldsymbol{0} \\ \boldsymbol{0} & \boldsymbol{0} & \boldsymbol{M}_m^* \end{bmatrix} \begin{bmatrix} \dot{\boldsymbol{v}}_c \\ \dot{\boldsymbol{h}}_c^r \\ \ddot{\boldsymbol{q}} \end{bmatrix} + \begin{bmatrix} \boldsymbol{C}_c & \boldsymbol{C}_{cr} & \boldsymbol{C}_{cm} \\ -\boldsymbol{C}_{cr}^T & \boldsymbol{C}_r^* & \boldsymbol{C}_{rm}^* \\ -\boldsymbol{C}_{cm}^T & -\boldsymbol{C}_{rm}^{*T} & \boldsymbol{C}_m^* \end{bmatrix} \begin{bmatrix} \boldsymbol{v}_c \\ \boldsymbol{h}_c^r \\ \dot{\boldsymbol{q}} \end{bmatrix} = \begin{bmatrix} \boldsymbol{f}_c \\ \boldsymbol{a}_c \\ \bar{\boldsymbol{\tau}} \end{bmatrix} + \begin{bmatrix} \boldsymbol{f}_{ext,c} \\ \boldsymbol{a}_{ext,c} \\ \bar{\boldsymbol{\tau}}_{ext} \end{bmatrix}. \tag{15}$$

where

$$\boldsymbol{M}_m^* = \boldsymbol{M}_m - \begin{bmatrix} \boldsymbol{M}_{tm}^T & \boldsymbol{M}_{rm}^T \end{bmatrix} \begin{bmatrix} \boldsymbol{M}_t & \boldsymbol{M}_{tr} \\ \boldsymbol{M}_{tr}^T & \boldsymbol{M}_r \end{bmatrix}^{-1} \begin{bmatrix} \boldsymbol{M}_{tm} \\ \boldsymbol{M}_{rm} \end{bmatrix} \in \mathbb{R}^{n \times n} \tag{16}$$

is the reduced inertia of the manipulator.
Expressing the dynamics in these new variables enables to obtain a system of inertially decoupled dynamic equations. Moreover, it can be demonstrated (see the Appendix) that the following relations hold:

$$\boldsymbol{C}_c \boldsymbol{v}_c + \boldsymbol{C}_{cr} \boldsymbol{h}_c^r + \boldsymbol{C}_{cm} \dot{\boldsymbol{q}} = m \left[\boldsymbol{\omega}_b\right]^\wedge \boldsymbol{v}_c, \tag{17a}$$

$$-\boldsymbol{C}_{cr}^T \boldsymbol{v}_c + \boldsymbol{C}_r^* \boldsymbol{h}_c^r + \boldsymbol{C}_{rm}^* \dot{\boldsymbol{q}} = \boldsymbol{I}_c^{-1} \left[\boldsymbol{\omega}_b\right]^\wedge \boldsymbol{h}_c^r, \tag{17b}$$

$$-\boldsymbol{C}_{cm}^T \boldsymbol{v}_c - \boldsymbol{C}_{rm}^{*T} \boldsymbol{h}_c^r + \boldsymbol{C}_m^* \dot{\boldsymbol{q}} = (\dot{\boldsymbol{M}}_m^* - \frac{1}{2} \boldsymbol{M}_{m/q}^*) \dot{\boldsymbol{q}} + (\dot{\bar{\boldsymbol{J}}}_\omega^T - \bar{\boldsymbol{J}}_\omega^T \left[\boldsymbol{\omega}_b\right]^\wedge + \frac{1}{2} \boldsymbol{I}_{c/q}^{-T} - \bar{\boldsymbol{J}}_{\omega/q}^T) \boldsymbol{h}_c^r, \tag{17c}$$

where

$$\begin{gathered} \boldsymbol{M}_{m/q}^* = \begin{bmatrix} \dot{\boldsymbol{q}}^T \frac{\partial \boldsymbol{M}_m^*}{\partial q_1} \\ \vdots \\ \dot{\boldsymbol{q}}^T \frac{\partial \boldsymbol{M}_m^*}{\partial q_n} \end{bmatrix} \in \mathbb{R}^{n \times n}, \quad \boldsymbol{I}_{c/q}^{-T} = \begin{bmatrix} \boldsymbol{h}_c^{rT} \frac{\partial \boldsymbol{I}_c^{-T}}{\partial q_1} \\ \vdots \\ \boldsymbol{h}_c^{rT} \frac{\partial \boldsymbol{I}_c^{-T}}{\partial q_n} \end{bmatrix} \in \mathbb{R}^{n \times 3}, \\ \bar{\boldsymbol{J}}_{\omega/q}^T = \begin{bmatrix} \dot{\boldsymbol{q}}^T \frac{\partial \bar{\boldsymbol{J}}_\omega^T}{\partial q_1} \\ \vdots \\ \dot{\boldsymbol{q}}^T \frac{\partial \bar{\boldsymbol{J}}_\omega^T}{\partial q_n} \end{bmatrix} \in \mathbb{R}^{n \times 3}. \end{gathered} \tag{18}$$

In the Appendix, a way to compute the partial derivatives of $\boldsymbol{M}_m^*$, $\boldsymbol{I}_c^{-T}$ and $\boldsymbol{J}_\omega^T$ with respect to $\boldsymbol{q}$ is explained.
By using the simplifications in (17), the dynamic equations can be rewritten as

$$m \dot{\boldsymbol{v}}_c + m \left[\boldsymbol{\omega}_b\right]^\wedge \boldsymbol{v}_c = \boldsymbol{f}_c + \boldsymbol{f}_{ext,c}, \tag{19a}$$

$$\dot{\boldsymbol{h}}_c^r + \left[\boldsymbol{\omega}_b\right]^\wedge \boldsymbol{h}_c^r = \boldsymbol{m}_c + \boldsymbol{m}_{ext,c}, \tag{19b}$$

$$\boldsymbol{M}_m^* \ddot{\boldsymbol{q}} + (\dot{\boldsymbol{M}}_m^* - \frac{1}{2} \boldsymbol{M}_{m/q}^*) \dot{\boldsymbol{q}} + (\dot{\bar{\boldsymbol{J}}}_\omega^T - \bar{\boldsymbol{J}}_\omega^T \left[\boldsymbol{\omega}_b\right]^\wedge + \frac{1}{2} \boldsymbol{I}_{c/q}^{-T} - \bar{\boldsymbol{J}}_{\omega/q}^T) \boldsymbol{h}_c^r = \bar{\boldsymbol{\tau}} + \bar{\boldsymbol{\tau}}_{ext}, \tag{19c}$$

where it is denoted $\boldsymbol{m}_c = \boldsymbol{I}_c \boldsymbol{a}_c \in \mathbb{R}^3$ and $\boldsymbol{m}_{ext,c} = \boldsymbol{I}_c \boldsymbol{a}_{ext,c} \in \mathbb{R}^3$.
First, note that Eqs. (19b) and (19c) do not depend on the base linear velocity anymore. On the other hand, Eq. (19a) depends on the base linear velocity through $\boldsymbol{v}_c$. Second, note that $\boldsymbol{M}_m^*$ and $\bar{\boldsymbol{J}}_\omega$ depend only on $\boldsymbol{q}$, $\boldsymbol{M}_{m/q}^*$, $\bar{\boldsymbol{J}}_{\omega/q}$, and $\dot{\bar{\boldsymbol{J}}}_\omega$ depends on $\boldsymbol{q}$ and $\dot{\boldsymbol{q}}$, and $\boldsymbol{I}_{c/q}^{-T}$ depends on $\boldsymbol{q}$, $\dot{\boldsymbol{q}}$, and $\boldsymbol{\omega}_b$.

Starting from (19), the residuals $\hat{\boldsymbol{f}}_{ext,c}, \hat{\boldsymbol{m}}_{ext,c} \in \mathbb{R}^3$ and $\hat{\bar{\boldsymbol{\tau}}}_{ext} \in \mathbb{R}^n$, are designed as

$$\hat{\boldsymbol{f}}_{ext,c} = \boldsymbol{K}_f(\underbrace{m\boldsymbol{v}_c}_{\boldsymbol{h}_c^t} - \int_0^t (\boldsymbol{f}_c - m\left[\boldsymbol{\omega}_b\right]^\wedge \boldsymbol{v}_c + \hat{\boldsymbol{f}}_{ext,c})ds), \tag{20a}$$

$$\hat{\boldsymbol{m}}_{ext,c} = \boldsymbol{K}_m(\boldsymbol{h}_c^r - \int_0^t (\boldsymbol{m}_c - \left[\boldsymbol{\omega}_b\right]^\wedge \boldsymbol{h}_c^r + \hat{\boldsymbol{m}}_{ext,c})ds), \tag{20b}$$

$$\hat{\bar{\boldsymbol{\tau}}}_{ext} = \boldsymbol{K}_\tau(\underbrace{\boldsymbol{M}_m^*\dot{\boldsymbol{q}}}_{\boldsymbol{h}_j^*} - \int_0^t (\bar{\boldsymbol{\tau}} + \frac{1}{2}\boldsymbol{M}_{m/q}^*\dot{\boldsymbol{q}} - (\dot{\bar{\boldsymbol{J}}}_\omega^T - \bar{\boldsymbol{J}}_\omega^T\left[\boldsymbol{\omega}_b\right]^\wedge + \frac{1}{2}\boldsymbol{I}_{c/q}^{-T} - \bar{\boldsymbol{J}}_{\omega/q}^T)\boldsymbol{h}_c^r + \hat{\bar{\boldsymbol{\tau}}}_{ext})ds), \tag{20c}$$

where $\boldsymbol{h}_j^* \in \mathbb{R}^n$ is the generalized momentum of the joints associated to the centroid-joints dynamics. By differentiating Eqs. (20a), (20b), and (20c), and by using the dynamics (19), the following equations result

$$\dot{\hat{\boldsymbol{f}}}_{ext,c} = \boldsymbol{K}_f(\boldsymbol{f}_{ext,c} - \hat{\boldsymbol{f}}_{ext,c}), \tag{21a}$$

$$\dot{\hat{\boldsymbol{m}}}_{ext,c} = \boldsymbol{K}_m(\boldsymbol{m}_{ext,c} - \hat{\boldsymbol{m}}_{ext,c}), \tag{21b}$$

$$\dot{\hat{\bar{\boldsymbol{\tau}}}}_{ext} = \boldsymbol{K}_\tau(\bar{\boldsymbol{\tau}}_{ext} - \hat{\bar{\boldsymbol{\tau}}}_{ext}), \tag{21c}$$

which express the relation between the estimated and true quantities. From Eq. (21), it is clear that $\hat{\boldsymbol{f}}_{ext,c}$, $\hat{\boldsymbol{m}}_{ext,c}$, and $\hat{\bar{\boldsymbol{\tau}}}_{ext}$ are first-order-filtered estimations of $\boldsymbol{f}_{ext,c}$, $\boldsymbol{m}_{ext,c}$, and $\bar{\boldsymbol{\tau}}_{ext}$, respectively. The observations about the gains tuning made in the previous section are also valid for the proposed observer.

Note that the residuals $\hat{\boldsymbol{m}}_{ext,c}$ and $\hat{\bar{\boldsymbol{\tau}}}_{ext}$ in (20b) and (20c) are computed without using the linear velocity. Indeed, $\boldsymbol{v}_b$ does not appear in (20b) and (20c), and the matrices therein are only function of $\boldsymbol{q}$, $\dot{\boldsymbol{q}}$, and $\boldsymbol{\omega}_b$, as remarked previously. This property has an important implication from the practical point of view. Considering real on-orbit scenarios, the linear velocity is not directly measured and its accurate estimation or reconstruction is difficult. Thanks to the decoupling from $\boldsymbol{v}_b$, the residuals $\hat{\boldsymbol{m}}_{ext,c}$ and $\hat{\bar{\boldsymbol{\tau}}}_{ext}$ can be computed just relying on gyroscopes, encoders and torque sensors, which typically feature good acquisition frequency and relatively low noise. Fast and accurate knowledge of the position and attitude of the base, and its velocity, which is often unpractical, is totally avoided. Then, the residuals $\hat{\boldsymbol{m}}_{ext,c}$ and $\hat{\bar{\boldsymbol{\tau}}}_{ext}$ can be exploited to reconstruct the external wrench $\boldsymbol{\mathcal{F}}_{ext}$ and to isolate the contact point, as it will be shown in the Sections 4 and 5, respectively.

4. Reconstruction of the external wrench

Assuming to know the contact point along the space robot, the relation between the contact generalized forces $\boldsymbol{f}_{ext,b}$, $\boldsymbol{m}_{ext,b}$, and $\boldsymbol{\tau}_{ext}$ in (2) and the external wrench $\boldsymbol{\mathcal{F}}_{ext}$ can be expressed as in Eq. (3). Using the inverse of Eq. (14) and recalling that $\boldsymbol{m}_{ext,c} = \boldsymbol{I}_c\boldsymbol{a}_{ext,c}$, the relation between $\boldsymbol{f}_{ext,c}$, $\boldsymbol{m}_{ext,c}$, and $\bar{\boldsymbol{\tau}}_{ext}$, and $\boldsymbol{\mathcal{F}}_{ext}$ is given by:

$$\begin{bmatrix} \boldsymbol{f}_{ext,c} \\ \boldsymbol{m}_{ext,c} \\ \bar{\boldsymbol{\tau}}_{ext} \end{bmatrix} = \begin{bmatrix} \boldsymbol{A}_{pc}^T \\ \boldsymbol{J}_p^{*T} \end{bmatrix} \boldsymbol{\mathcal{F}}_{ext}, \tag{22}$$

where

$$\boldsymbol{J}_p^* = \begin{bmatrix} \boldsymbol{J}_{vp}^* \\ \boldsymbol{J}_{\omega p}^* \end{bmatrix} = \begin{bmatrix} -\boldsymbol{R}_{pb}\bar{\boldsymbol{J}}_v + \boldsymbol{R}_{pb}[\boldsymbol{p}_{cp}]^\wedge \bar{\boldsymbol{J}}_\omega + \boldsymbol{J}_{vp} \\ -\boldsymbol{R}_{pb}\bar{\boldsymbol{J}}_\omega + \boldsymbol{J}_{\omega p} \end{bmatrix} \in \mathbb{R}^{6\times n}. \tag{23}$$

Then, an estimate $\hat{\boldsymbol{\mathcal{F}}}_{ext}$ of the external wrench at the end-effector can be computed as

$$\hat{\boldsymbol{\mathcal{F}}}_{ext} = \left(\begin{bmatrix} \boldsymbol{A}_{pc}^T \\ \boldsymbol{J}_p^{*T} \end{bmatrix} \right)^\# \begin{bmatrix} \hat{\boldsymbol{f}}_{ext,c} \\ \hat{\boldsymbol{m}}_{ext,c} \\ \hat{\bar{\boldsymbol{\tau}}}_{ext} \end{bmatrix}, \tag{24}$$

where the operator $(\cdot)^\#$ stands for the Moore-Penrose pseudo inverse of the argument.
Considering $\begin{bmatrix} \boldsymbol{A}_{pc}^T \\ \boldsymbol{J}_p^{*T} \end{bmatrix}$ has maximum rank, one has the freedom to eliminate redundant rows. In particular, the estimate of the external wrench can be obtained using only $\hat{\boldsymbol{m}}_{ext,c}$ and $\hat{\bar{\boldsymbol{\tau}}}_{ext}$, and thus getting rid of the base linear velocity. Selecting the last two rows of Eq. (22) and taking the pseudo inverse, the following relation can be written

$$\hat{\boldsymbol{\mathcal{F}}}_{ext} = \left(\tilde{\boldsymbol{J}}_p^{*T} \right)^\# \begin{bmatrix} \hat{\boldsymbol{m}}_{ext,c} \\ \hat{\bar{\boldsymbol{\tau}}}_{ext} \end{bmatrix}, \tag{25}$$

where

$$\tilde{\boldsymbol{J}}_p^{*T} = \begin{bmatrix} [\boldsymbol{p}_{cp}]^\wedge \boldsymbol{R}_{pb}^T & \boldsymbol{R}_{pb}^T \\ \boldsymbol{J}_{vp}^{*T} & \boldsymbol{J}_{\omega p}^{*T} \end{bmatrix} \in \mathbb{R}^{(n+3)\times 6}. \tag{26}$$

Clearly, the rank of $\tilde{\boldsymbol{J}}_p^*$ should be maximum to reconstruct $\hat{\boldsymbol{\mathcal{F}}}_{ext}$ correctly. Notice that by using Eq. (25), it is possible to estimate the external wrench acting at a generic known point along the robot without using any unpractical measurements, such as the base linear velocity or the joint accelerations.
In the development of the reconstruction strategy, the contact point has been assumed to be known. In case of a planned contact at the end-effector, this is true and, through the kinematics, it is straightforward to compute $\boldsymbol{p}_{ce}$ and the Jacobians $\boldsymbol{J}_{ve}$, $\boldsymbol{J}_{\omega e}$ (the generic point p coincides with the end-effector) required in Eq. (24) and in Eq. (25). Conversely, when dealing with an unexpected collision, the contat point is unknown and it is necessary to isolate it before being able to reconstruct the external wrench. In the following section, a solution to this problem is proposed.

5. Contact point isolation

Solving the isolation problem means locating the contact point p. In the following, first, a procedure to identify the contact point using all the residual vectors is presented. This procedure can be applied considering both the observer (5) and (20). Then, a different approach is proposed that relies only on $\hat{\boldsymbol{m}}_{ext,c}$ and $\hat{\bar{\boldsymbol{\tau}}}_{ext}$, avoiding the need of the base linear velocity knowledge. In the development of both strategies, it is assumed that the point of application of the external disturbance does not change during the contact, and the contact wrench only consists in a linear force and no torque, namely

$$\boldsymbol{\mathcal{F}}_{ext} = \begin{bmatrix} \boldsymbol{f}_{ext} \\ \boldsymbol{0} \end{bmatrix} \tag{27}$$

Note that these are reasonable assumptions for unexpected collisions.

5.1. Isolation using all the residual vectors

Considering all the residual vectors available, the contact point can be identified easily. Indeed, given (22) and the assumption (27), it is

$$\boldsymbol{m}_{ext,c} = [\boldsymbol{p}_{cp}]^{\wedge} \boldsymbol{f}_{ext,c}. \tag{28}$$

Then, it is possible to write

$$\hat{\boldsymbol{m}}_{ext,c} = [\boldsymbol{p}_{cp}]^{\wedge} \hat{\boldsymbol{f}}_{ext,c}, \tag{29}$$

which means that the contact point can be found on the line

$$\boldsymbol{s}_{cp} = (-[\hat{\boldsymbol{f}}_{ext,c}]^{\wedge})^{\#} \hat{\boldsymbol{m}}_{ext,c} + d \frac{\hat{\boldsymbol{f}}_{ext,c}}{||\hat{\boldsymbol{f}}_{ext,c}||} \in \mathbb{R}^3, \tag{30}$$

with d being a varying scalar.

At this point, the contact point can be identified as the intersection between $\boldsymbol{s}_{cp}$ and the space robot, whose CAD representation is known or can be simplified by primitive shapes. In order to discriminate the exact point among multiple possibilities, the estimation of the external torques can be exploited. Indeed, the exact point would be the one that minimizes $||\boldsymbol{J}_p^{*T} \hat{\boldsymbol{\mathcal{F}}}_{ext} - \hat{\bar{\boldsymbol{\tau}}}_{ext}||$. Note that the same procedure can be applied using the residuals in (5).

It can be observed that this method is very straightforward. However, as already pointed out, from a practical point of view it would be more convenient to be able to isolate the contact point without relying on the base linear velocity knowledge. For this reason in the following section a different approach is proposed.

5.2. Isolation using only $\hat{m}_{ext,c}$ and $\hat{\bar{\tau}}_{ext}$

Assuming that the link i, on which the contact occurred, is known, the external wrench $\boldsymbol{\mathcal{F}}_{ext}$ can be transformed with respect to a frame attached on a known position to link i using the Adjoint matrix, as

$$\boldsymbol{\mathcal{F}}_i = \begin{bmatrix} \boldsymbol{f}_i \\ \boldsymbol{m}_i \end{bmatrix} = \boldsymbol{A}_{pi}^T \boldsymbol{\mathcal{F}}_{ext} = \begin{bmatrix} \boldsymbol{E} & \boldsymbol{0} \\ [\boldsymbol{p}_{ip}]^{\wedge} & \boldsymbol{E} \end{bmatrix} \begin{bmatrix} \boldsymbol{f}_{ext} \\ \boldsymbol{0} \end{bmatrix}, \tag{31}$$

where $\boldsymbol{p}_{ip}$ is constant.

The effect of the contact wrench at frame i can be estimated using the recostruction strategy preaviously explained in Section 4 as

$$\hat{\boldsymbol{\mathcal{F}}}_i = \begin{bmatrix} \hat{\boldsymbol{f}}_i \\ \hat{\boldsymbol{m}}_i \end{bmatrix} = \left(\begin{bmatrix} [\boldsymbol{p}_{ci}]^{\wedge} \boldsymbol{R}_{ib}^T & \boldsymbol{R}_{ib}^T \\ \boldsymbol{J}_{vi}^{*T} & \boldsymbol{J}_{\omega i}^{*T} \end{bmatrix} \right)^{\#} \begin{bmatrix} \hat{\boldsymbol{m}}_{ext,c} \\ \hat{\bar{\boldsymbol{\tau}}}_{ext} \end{bmatrix} \tag{32}$$

where $\boldsymbol{J}_{vi}^*$, $\boldsymbol{J}_{\omega i}^*$ can be computed substituting in Eq. (23) $\boldsymbol{R}_{pb}$ with $\boldsymbol{R}_{ib}$, $\boldsymbol{p}_{cp}$ with $\boldsymbol{p}_{ci}$, and $\boldsymbol{J}_{vp}$, $\boldsymbol{J}_{\omega p}$ with the Jacobians mapping $\dot{\boldsymbol{q}}$ into the linear and angular velocity of frame i. At this point, manipulating Eq. (31), the following relation can be written

$$\hat{\boldsymbol{m}}_i = [\boldsymbol{p}_{ip}]^{\wedge} \hat{\boldsymbol{f}}_i, \tag{33}$$

from which the line of action of $\boldsymbol{f}_{ext}$ can be computed as

$$\boldsymbol{s}_{ip} = (-[\hat{\boldsymbol{f}}_i]^{\wedge})^{\#} \hat{\boldsymbol{m}}_i + d_i \frac{\hat{\boldsymbol{f}}_i}{||\hat{\boldsymbol{f}}_i||} \in \mathbb{R}^3. \tag{34}$$

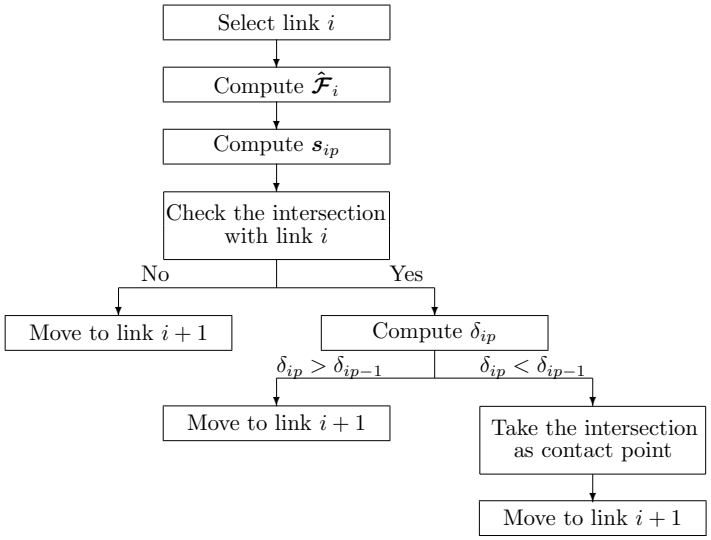

Figure 2: Scheme of the proposed isolation method.

with d_i being a varying scalar. Assuming the knowledge of the geometry of the link i, the contact point can be found as the intersection bewteen the link and the line $\boldsymbol{s}_{ip}$.

Unfortunately, the contact link is usually not known in advance. However, it is possible to overcome this issue. Indeed, the scheme just explained can be applied to each link, assuming that the link is the contact one. At the end, two possible results can be obtained:

- no intersections are found between the line of action and the link;
- a candidate contact point is found.

Among all the candidate points, the real contact point is the one minimizing

$$\delta_{ip} = \left\| \tilde{\boldsymbol{J}}_{p,i}^{*T} \begin{bmatrix} \hat{\boldsymbol{f}}_{ext} \\ \boldsymbol{0} \end{bmatrix} - \begin{bmatrix} \hat{\boldsymbol{m}}_{ext,c} \\ \hat{\tilde{\boldsymbol{\tau}}}_{ext} \end{bmatrix} \right\|, \tag{35}$$

where $\tilde{\boldsymbol{J}}_{p,i}^{*T} \in \mathbb{R}^{6\times(n+3)}$ is the Jacobian at the candidate point on link i. Fig. 2 reports the isolation method schematically.

To conclude, the residuals $\hat{\boldsymbol{m}}_{ext,c}$ and $\hat{\tilde{\boldsymbol{\tau}}}_{ext}$ allow not only to detect and estimate a contact force, but also to isolate it without the need of the knowledge of the base linear velocity.

6. Simulation example

In this section, the two observers are compared through numerical simulations including realistic noise models for the measurements. The linear velocity of the base is reconstructed using a kinematics-based Kalman filter. The superior performance and the advantages of the proposed method based on the centroid-joints dynamics are shown.

Table 1: Kinematics and dynamics parameters.

	l [m]	m [kg]	I_x [kgm^2]	I_y [kgm^2]	I_z [kgm^2]
Base	1.2	375	280	165	250
Link 1	0.17	5.1	0.03	0.03	0.03
Link 2	1.3	18.8	1.65	1.65	0.64
Link 3	0.17	8.9	0.15	0.15	0.03
Link 4	1.3	12.0	0.25	0.25	0.03
Link 5	0.17	11.7	0.26	0.26	0.03
Link 6	0.1	5.5	0.02	0.02	0.03
Link 7	0	4.7	0.01	0.01	0.02

6.1. Simulation scenario

A 7DoF manipulator mounted on a 6DoF floating base is considered. The kinematics and dynamics parameters are reported in Tab. 1.

The base is controlled to keep the initial attitude through a PD controller, whereas it is free to translate, i.e., $\boldsymbol{f}_b = \boldsymbol{0}$. The manipulator joints are controlled to follow a reference trajectory. Especially, joint 1 and joint 4 are commanded to follow a trapezoidal velocity profile, while the other joints are commanded to keep the initial position, i.e., $\boldsymbol{q}_0 = [-3 \;\; 30 \;\; 0 \;\; 130 \;\; 0 \;\; -60 \;\; 0]^T$ deg. A simple PD controller is implemented for each joint. Note that the performance of both contact observers does not depend on the control strategy adopted. A constant external wrench is applied at the end-effector between $t = 2.5$ s and $t = 3.5$ s. The wrench consists of only a linear force, with value $\boldsymbol{f}_{ext} = [-10 \; 5 \; 8]^T$ N, and no torque.

6.2. Measurement model and velocity reconstruction

The angular velocity, the joint angles and the joint torques can be directly measured using a gyro, encoders and joint torque sensors, respectively. On the other hand, the linear velocity, required for the contact wrench reconstruction only by the observer (5), and the joint velocities, required by both observers, are not directly measured but need to be reconstructed, either using a discrete derivative or by data fusion. Herein only the problem of the estimation of the linear velocity is addressed, while a simplified noise performance model is used for the joint velocities.

In order to compare the observers with similar noise conditions, the measurements of the angular velocity, joint angles and joint velocities are assumed to be affected by a white Gaussian noise with zero mean, while an uniform noise is considered for the torque sensors [13]. For the angular velocity a bias is also introduced leading to the following model [22]:

$$\begin{aligned} \boldsymbol{\omega}_b^m &= \boldsymbol{\omega}_b + \boldsymbol{b}_\omega + \boldsymbol{\eta}_\omega \\ \dot{\boldsymbol{b}}_\omega &= \boldsymbol{\eta}_{b\omega}, \end{aligned} \tag{36}$$

where $\boldsymbol{\omega}_b^m \in \mathbb{R}^3$ is the measured angular velocity of the base; the term $\boldsymbol{b}_\omega \in \mathbb{R}^3$ is the bias; the terms $\boldsymbol{\eta}_\omega, \boldsymbol{\eta}_{b\omega} \in \mathbb{R}^3$ are white Gaussian noise with zero mean.

The linear velocity is reconstructed through a kinematics-based Kalman filter using a gyro and an accelerometer in the prediction step, and camera measurements for the update step. These sensors are placed on the spacecraft. The camera measures the position of the inertial frame $\mathcal{T}$, that can be imagined to be located on a target object, with respect to the base (see Fig. 1).

The position of the target with respect to the base $\boldsymbol{p}_{bt} \in \mathbb{R}^3$ and base velocity $\boldsymbol{v}_b$, expressed in $\mathcal{B}$, compose the state vector, and their time derivatives are

$$\begin{aligned} \dot{\boldsymbol{p}}_{bt} &= -[\boldsymbol{\omega}_b]^\wedge \boldsymbol{p}_{bt} - \boldsymbol{v}_b, \\ \dot{\boldsymbol{v}}_b &= -[\boldsymbol{\omega}_b]^\wedge \boldsymbol{v}_b + \boldsymbol{a}_b, \end{aligned} \tag{37}$$

Table 2: Standard deviations and biases of the considered noise model.

σ_q [rad]	$\sigma_{\dot{q}}$ [rad/s]	σ_τ [Nm]	$\sigma_{p_{bt}}$ [m]	$\sigma_{b\omega}$ [μrad/s$^{3/2}$]
$5 \cdot 10^{-5}$	10^{-4}	0.2	0.01	$3.162 \cdot 10^{-4}$

σ_ω [μrad/s$^{1/2}$]	σ_{ba} [m/s$^{5/2}$]	σ_a [m/s$^{3/2}$]	$b_{\omega,0}$ [rad/hr]	$b_{a,0}$ [m/s^2]
0.316	$6.00 \cdot 10^{-5}$	$9.81 \cdot 10^{-5}$	0.0017	0.003

where $\boldsymbol{a}_b \in \mathbb{R}^3$ is the base acceleration. Eq. (37) is the prediction step of the filter, where $\boldsymbol{\omega}_b$ and $\boldsymbol{a}_b$ are measured by the inertial measurement unit (IMU), including the gyro and the accelerometer.
The measurement equation is

$$\tilde{\boldsymbol{p}}_{bt} = \boldsymbol{p}_{bt}, \tag{38}$$

where $\tilde{\boldsymbol{p}}_{bt} \in \mathbb{R}^3$ is the measurement vector.
Also for the accelerometer, the noise model (36) is used [23]. On the other hand, for the camera, the noise is introduced by adopting the exponentially correlated random variable model [24][25]

$$\begin{aligned} \epsilon_{k+1} &= K\epsilon_k + \sqrt{1-K^2}\mathcal{N}(0,\sigma), \\ K &= e^{-1/(f_a T)}, \end{aligned} \tag{39}$$

where ϵ is the error with respect to the true quantity, $\mathcal{N}(0,\sigma)$ is a random number generated with a normal distribution of zero mean and standard deviation σ, f_a is the acquisition frequency and T is the autocorrelation time.
The standard deviations and biases of the considered noise models are reported in Tab. 2. The camera acquires measurements at 3 Hz, while all the other sensors work at 200 Hz. The filter prediction step is performed at 200 Hz, whereas the update step at 3 Hz. Note that the attitude is controlled to be fixed. To achieve this goal, attitude measurements are necessary, and thus it is assumed that the spacecraft is equipped with a star tracker, which measures the Euler angles $\boldsymbol{\Phi} \in \mathbb{R}^3$. The exponentially correlated random variable model (39) is used to reproduce the noise of the sensor [24], with standard deviation $\sigma_\Phi = 1.04 \cdot 10^{-4}$ rad. The star tracker works at 3 Hz, while the controller works at 200 Hz. Hence, the extended Kalman filter for quaternions presented in [26] is implemented [2]. Similar to the filter for the base velocity, the prediction is run at 200 Hz, while the update at 3 Hz.

6.3. Observers comparison

In [19] the better performance of the proposed method based on a centroid-joints dynamics are shown considering a simplified Gaussian noise model for the linear velocity. In that case, the noise on consecutive measurements is completely uncorrelated and this feature deteriorates significantly the performance of the observer (5), and consequently the accuracy of the external wrench estimation. In this paper, the linear velocity is estimated through a Kalman filter, and thus it turns out to be less noisy. However, after the filter has converged, the estimation is still affected by a certain level of uncertainty. When the prediction is updated, at a frequency of 3 Hz, the velocity estimate may vary suddenly of few mm/s. This is due to the fact that the prediction step runs at a higher frequency and the error in the predicted states is accumulated. These

[2] In [26] the filter estimates also the angular velocity and the measurements are acquired by a laser vision system. In this work, only the attitude is estimated and the measurements are provided by the star tracker, but the implementation of the filter is analogous.

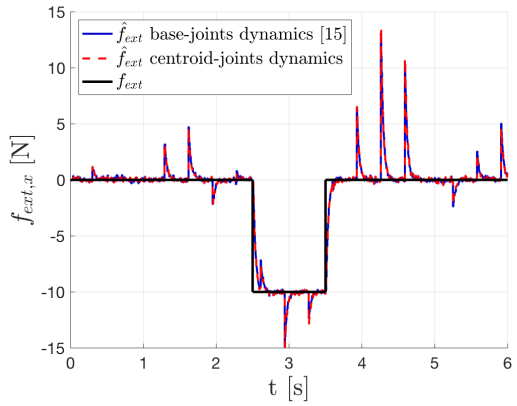

Figure 3: Comparison between the observer [15] and the proposed one, including $\hat{\boldsymbol{f}}_{ext,b}$ and $\hat{\boldsymbol{f}}_{ext,c}$ in the estimation process.

sudden variations in the correction phase affect significantly the computation of the residuals depending on the linear velocity, namely all the ones in (5) and $\hat{\boldsymbol{f}}_{ext,c}$. Consequently, the accuracy of the contact wrench reconstruction deteriorates. To mitigate this issue, the observers gains should be decreased considerably, limiting the bandwidth. Conversely, the issue is overcome if the external wrench is estimated through (25), since $\hat{\boldsymbol{m}}_{ext,c}$ and $\hat{\tilde{\boldsymbol{\tau}}}_{ext}$ are decoupled from the base linear velocity. Before proceeding, note that, in this simulation, the contact point is at the end-effector, and thus it is assumed to be known.

Figs. 3 and 4 show a comparison between the reviewed method [15] and the proposed one. Fig. 3 compares the two methods when all the three residuals are used to reconstruct $\boldsymbol{f}_{ext}$. Only one component of the force is reported, but similar results are obtained for the other two. In this case, for the observer based on a base-joints dynamics, i.e., given by (5), a contact force estimate $\hat{\boldsymbol{f}}_{ext}$ is computed by taking the pseudo inverse of the relation (3) and using the residuals $\hat{\boldsymbol{f}}_{ext,b}$, $\hat{\boldsymbol{m}}_{ext,b}$, and $\hat{\boldsymbol{\tau}}_{ext}$, whereas for the observer (20) it is given by the relation (24). On the other hand, Fig. 4 compares the two methods when only the angular and joint momentum residuals are used to reconstruct $\boldsymbol{f}_{ext}$. For the observer (5), the contact force estimate $\hat{\boldsymbol{f}}_{ext}$ is computed removing the first row of (3), i.e., without $\hat{\boldsymbol{f}}_{ext,b}$, and by taking the pseudo inverse of the resulting relation, while for the observer (20) it is given by the relation (25), i.e., without $\hat{\boldsymbol{f}}_{ext,c}$. In both observers, all the gains are set equal to 30 s^{-1}.

Fig. 3 shows that the estimation process is significantly affected by the uncertainty in the linear velocity and both observers provide similar bad performance. This is caused by the residuals $\hat{\boldsymbol{f}}_{ext,b}$ and $\hat{\boldsymbol{f}}_{ext,c}$, which are the ones mostly affected by the explained issue.

On the other hand, the simulation shown in Fig. 4, in which $\hat{\boldsymbol{f}}_{ext,b}$ and $\hat{\boldsymbol{f}}_{ext,c}$ are not used in the estimation process, highlights the advantage of using the proposed observer based on the centroid-joints dynamics. Indeed, it provides a definitely more accurate estimate of the external force, especially during the contact. It is worth stressing that the superior performance of the proposed method derives from the complete decoupling of $\hat{\boldsymbol{m}}_{ext,c}$ and $\hat{\tilde{\boldsymbol{\tau}}}_{ext}$ from the linear velocity $\boldsymbol{v}_b$. The estimation through (25) turns out to be more practical and robust since it requires the use of only reliable, high-rate, and accurate direct measurements, as the ones provided by gyros, encoders and torque sensors. Moreover, the capability of these sensors of working at high rate, allow achieving high observer bandwidths and thus faster contact detection. The estimation based on a centroid-joints dynamics does not depend on the performance of the filter which can even deteriorates due to occlusions of the camera or adverse light conditions, here not simulated.

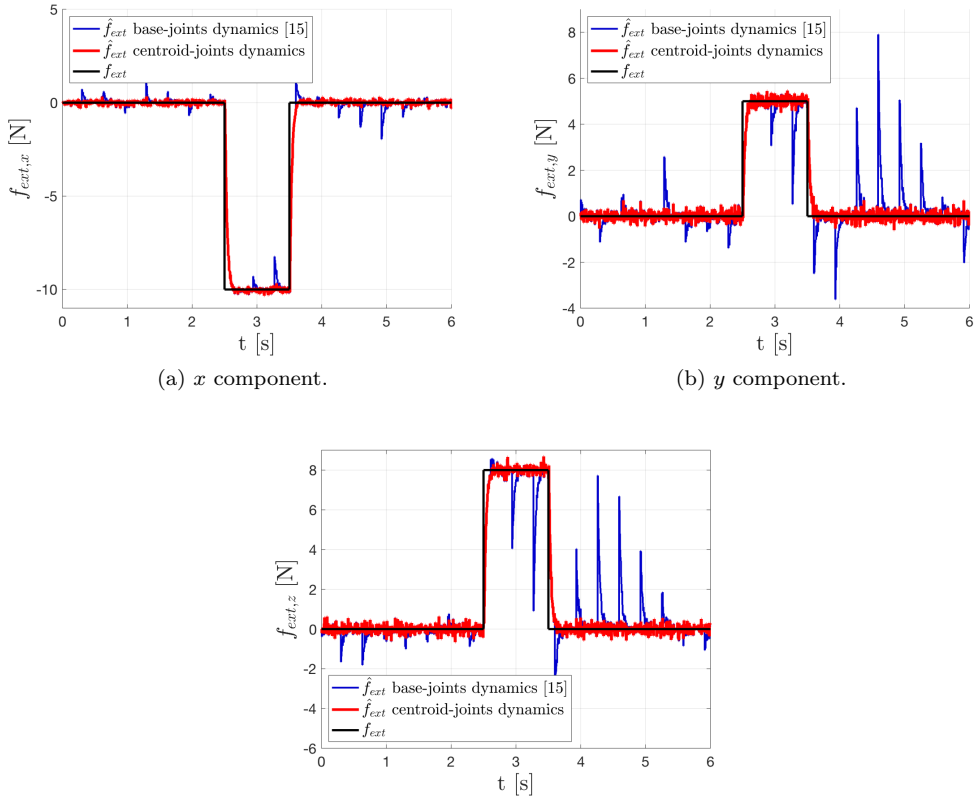

(a) x component.

(b) y component.

(c) z component.

Figure 4: Comparison between the observer [15] and the proposed one, without using $\hat{\boldsymbol{f}}_{ext,b}$ and $\hat{\boldsymbol{f}}_{ext,c}$ in the estimation process.

Finally, the residuals $\hat{\boldsymbol{m}}_{ext,c}$ and $\hat{\tilde{\boldsymbol{\tau}}}_{ext}$ turn out to be more adequate monitoring signals for the detection of the contact. Indeed, they are less prone to false positive than the residuals in (5), which show some spikes (visible in Fig. 4 in the force reconstruction) due to the uncertainty in the linear velocity estimation.

6.4. Reconstruction of the contact force on a generic point

In this section, it is shown that the proposed observer based on a centroid-joint dynamics can be used to detect and reconstruct a contact force acting on a generic point along the robot. First, the contact is detected using the residuals $\hat{\boldsymbol{m}}_{ext,c}$ and $\hat{\tilde{\boldsymbol{\tau}}}_{ext}$. Then, in order to estimate the force, the contact point is isolated through the method explained in Section 5. Finally, the external force is estimated using Eq. (25). The space robot is commanded to keep the initial attitude and manipulator's configuration, i.e., $\boldsymbol{q}_0 = [0\ 40\ 0\ 110\ 0\ 45\ 0]$ deg. Similarly to the previous case, a constant external wrench is applied between $t = 2.5$ s and $t = 3.5$ s and it consists of only a linear force $\boldsymbol{f}_{ext} = [-10\ 5\ 8]$ N and no torque. In this case, the external wrench acts on a mid-section on the link 4. In this simulation, the observer's gains are set equal to 20 s^{-1}.
The contact point is isolated with a maximum error norm of 4 cm, which is acceptable for a good recontruction

of the contact force. Then, Eq. (25) is used to estimate the contact force $\boldsymbol{f}_{ext}$. Fig. 5 shows that the proposed method provides good estimation performance even in the case of a contact on a generic point along the robot.

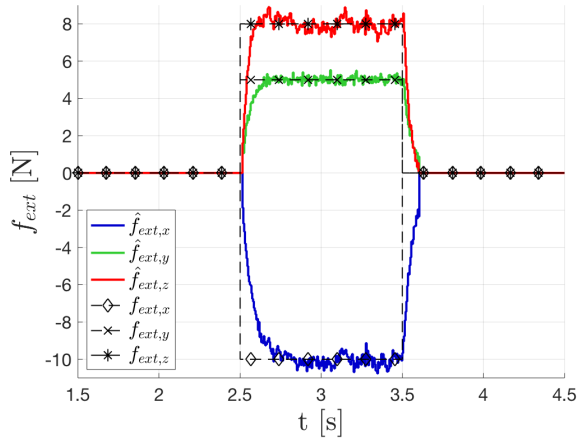

Figure 5: Reconstruction of the external force acting on a generic point along the robot.

7. Experimental validation

Both observers (5) and (20) have been validated on the On-Orbit Servicing Simulator (OOS-Sim) hardware-in-the-loop facility [18] at the DLR. This is a robotic simulator reproducing the in-orbit dynamics of a space robot. Thanks to the OOS-Sim, it is possible to test the algorithms, which will run on the space robot, on ground, before the actual deployment in orbit. The facility is made up of two parts (see Fig. 6): a simulator arm and a test arm. The former one is a position-controlled KUKA KR120 industrial robot on top of which a mock-up of a satellite is mounted. The simulator arm reproduces the spacecraft's dynamics based on a real-time model integration. The test arm is a KUKA KR4+ lightweight robot with seven degrees of freedom, which is equipped with torque sensors and can be controlled both in position and torque. In the test arm, the joint gravity torques are compensated based on an identified model, thereby replicating the microgravity conditions. Note that in this way the observers are validated taking into account real dynamics, sensor noise, time delay, discretization, and model uncertainties of the test arm. On the other hand, the dynamics of the spacecraft is simulated based on a model, and its states are reconstructed from the forward kinematics of the KUKA KR120 industrial robot. The satellite parameters can be adapted depending on the scenario. In this study, they are $m = 150$ kg, $I_x = 21.8$ kgm^2, $I_y = 15.0$ kgm^2, and $I_z = 18.88$ kgm^2. The simulated dynamics runs on a Linux real-time computer at 4 ms, while the space robot controller runs on a separate Linux real-time computer at 1 ms. The dynamics matrices used in the observers' implementation are computed at 5 ms. Further information on the facility setup and model integration can be found in [10][18]. Since the satellite's dynamics is simulated and its state reconstructed, they feature very low level of noise and uncertainties compared to the ones expected in space. For this reason, the experiments here presented are relevant to validate the applicability of the observers on real hardware, but not to compare them. Indeed, as already shown via simulation results, the better performance of the proposed method are evident when more realistic noise conditions for the spacecraft's states acquisition are considered. Finally, it

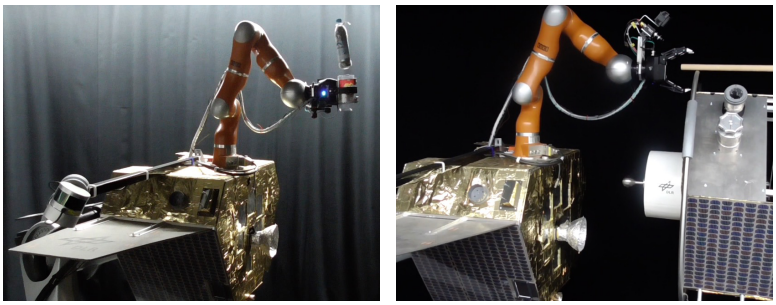

(a) Experiment with a known force. (b) Experiment with consecutive contacts.

Figure 6: Pictures of the experimental tests on the OOS-Sim hardware-in-the-loop facility.

is pointed out that the observer based on a base-joints dynamics [15] has not been tested on real hardware so far.

In order to verify the accuracy of the observers, first, an experiment in which a known constant force is applied at the end-effector has been performed. Then, the end-effector has been hit multiple times simulating a condition in which consecutive contacts occur close in time, and the correct behavior of the observers is checked. In both experiments, a compliant controller is implemented to control the end-effector position, the space robot's CM and the base attitude. A complete description of the control method is reported in [27].

7.1. Experiments with a known force

In these experiments, the gripper mounted on the test manipulator holds a container initially empty. A known mass is laid down in the container and it is removed after a certain time (see Fig. 6a). The resulting action on the space robot is a step-like constant disturbance force acting at the end-effector along the gravity direction. Especially, the disturbance force in the inertial frame is equal to $\boldsymbol{f}_{ext,t} = [0\ 0\ -8.373]^T$ N. The observers are required to reconstruct this force correctly. In both observers, the gains are set equal to $30\ \mathrm{s}^{-1}$. Figs. 7a and 7b show the reconstruction of the external force, expressed in $\mathcal{E}$[3], by the observers (5) and (20), respectively, using all the residuals. Both the observers are able to estimate the external wrench accurately and no significant differences can be noticed between them. When the mass is laid down and then removed, it can be noticed a small peak along the z direction of the end-effector frame. This can be explained by the fact that during these two phases the mass hits the container's wall along that direction, providing a small force.

In Figs. 8a and 8b, the results using only the joint and angular momentum residuals in the estimation process are reported, for the observers (5) and (20), respectively. Again, the observers show a similar behavior. They estimate the external force satisfactorily. It can be noticed that the accuracy decreases with respect to the estimation using all the residual vectors. This is due to the fact that the gravity disturbance, affecting the test arm, is not compensated exactly because of uncertainties in the gravity model used for the compensation. Therefore, this introduces an error in the estimates $\hat{\boldsymbol{\tau}}_{ext}$ and $\hat{\bar{\boldsymbol{\tau}}}_{ext}$ which is propagated to the estimate $\hat{\boldsymbol{f}}_{ext}$. In the previous case, Figs. 7a and 7b, this error is mitigated by using the translational momentum residuals

[3]Note that in the experiment the y direction of the $\mathcal{E}$ frame is almost aligned with the -z direction of the inertial frame.

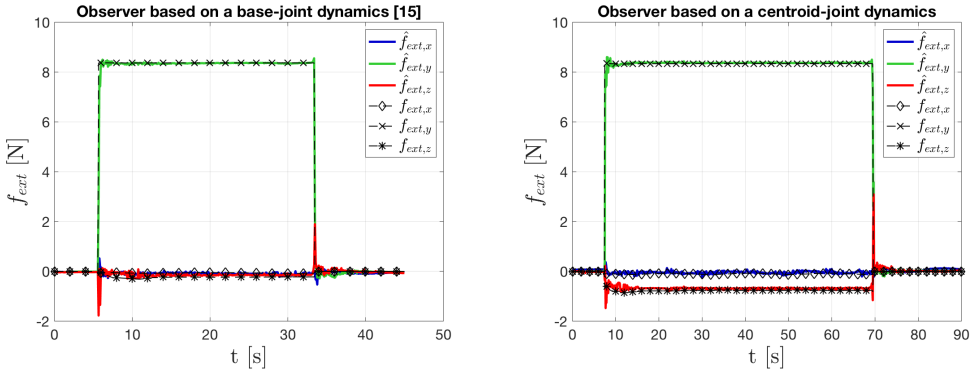

(a) Observer [15]. (b) Proposed observer.

Figure 7: External force estimate including $\hat{\boldsymbol{f}}_{ext,b}$ and $\hat{\boldsymbol{f}}_{ext,c}$ in the estimation process.

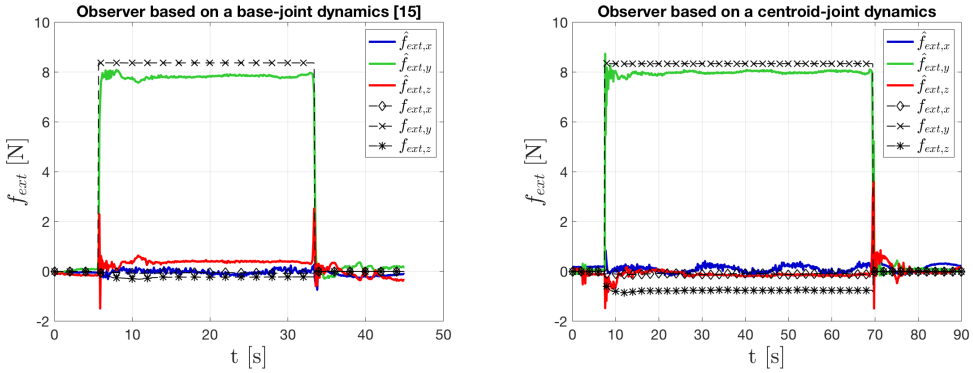

(a) Observer [15]. (b) Proposed observer.

Figure 8: External force estimate without including $\hat{\boldsymbol{f}}_{ext,b}$ and $\hat{\boldsymbol{f}}_{ext,c}$ in the estimation process.

in the estimation process, which is a direct estimate of the force, and thus introduces further information in the reconstruction. Note that this error is induced by the simulation facility via its artificial model-based compensation of the terrestrial gravity torques. This effect is not present in orbit, in which the robot acts in true microgravity conditions.

The present experiment validates the applicability of the observers (5) and (20) when considering a real arm. No spacecraft sensors are simulated in the current experiments, thus the experiment does not reproduce the advantage of the observer (20) in presence of measurement noise, which was validated via numerical simulation. Thus, it is remarked that the experimental results cannot be used for comparing the noise behavior of the observers. In future work the experiments will be repeated with sensor models.

7.2. Experiment with consecutive contacts

In this experiment, the test arm was hit with a stick multiple times at the end-effector along different directions (see Fig. 6b). Short and long contacts were simulated and the behavior of the observers was analyzed. Only the results related to the observer (20) are reported here, for the sake of brevity. However, similar results were obtained for the observer (5). The gains for the computation of the translational and angular momentum residuals were set equal to 30 s^{-1}, while they were increased to 100 s^{-1} for the joint momentum residuals.

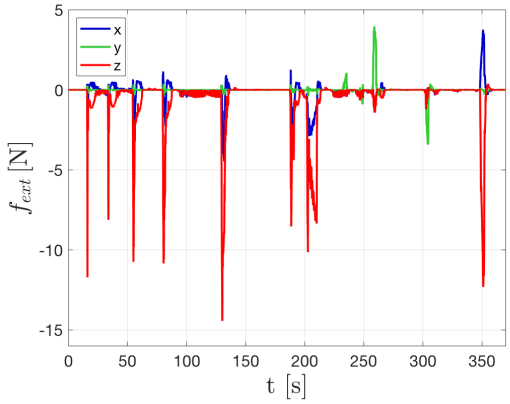

Figure 9: Force at the end-effector of the test arm in the consecutive contacts experiment.

The direction of the impacts can be seen in Fig. 9, which shows the reconstructed contact force at the end-effector, expressed in $\mathcal{E}$. In Figs. 10b and 10c the residuals $\hat{\boldsymbol{f}}_{ext,c}$ and $\hat{\boldsymbol{m}}_{ext,c}$ are reported. It can be noted that, when the force is mostly along the z direction of the end-effector frame, the contact can be easily detected on the x and z components of $\hat{\boldsymbol{f}}_{ext,c}$ and on the y component of $\hat{\boldsymbol{m}}_{ext,c}$. On the other hand, between $t = 230$ s and $t = 330$ s, the external force acts along the y-axis of $\mathcal{E}$ and the contact can be detected on the y component of $\hat{\boldsymbol{f}}_{ext,c}$ and on the x and z components of $\hat{\boldsymbol{m}}_{ext,c}$. Finally, Fig. 10a illustrates the residuals $\hat{\bar{\boldsymbol{\tau}}}_{ext}$. The contacts are detected mostly by the monitoring signals at the first four joints, while the other three remain around zero. Especially, the contacts along the z-axis of $\mathcal{E}$ are detected by the signals at joint 2 and joint 4. Conversely, the contacts along the y-axis of $\mathcal{E}$ are seen by the signals at joint 1 and joint 3.

8. Conclusions

In this paper, the problem of estimating a contact wrench acting on a generic point along a space robot was addressed. The observer presented in [15] was reviewed and analyzed considering the issues related to a space robot. Then, a new observer was proposed introducing a new set of generalized velocities, including the linear velocity of the spacecraft-manipulator's CM, the angular momentum around the CM and the joint velocities. This observer turned out to provide a more accurate estimation of the external wrench when realistic noise conditions are considered. Indeed, the new angular and joint momentum residuals can be used to isolate and estimate the contact relying only on accurate sensors working at high frequency, since they do not depend on the base linear velocity. The superior performance of the proposed method was shown through a simulation example, including realistic measurement noise and the reconstruction of the base linear velocity using a

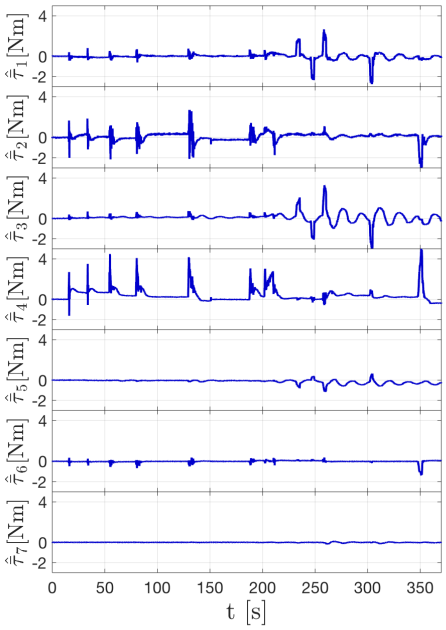

(a) Joints momentum residuals $\hat{\tilde{\boldsymbol{\tau}}}_{ext}$.

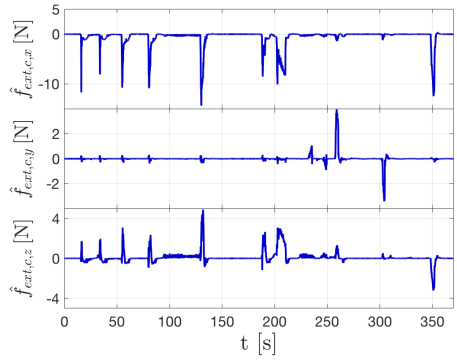

(b) Translation momentum residuals $\hat{\boldsymbol{f}}_{ext,c}$.

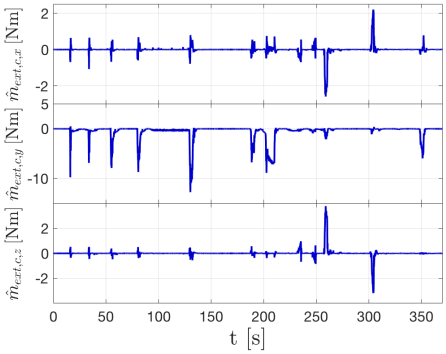

(c) Angular momentum residuals $\hat{\boldsymbol{m}}_{ext,c}$.

Figure 10: Momentum residuals of the proposed observer in the consecutive contacts experiment.

Kalman filter. Finally, the applicability of both observers on hardware was successfully validated using the the OOS-Sim hardware-in-the-loop facility at the DLR.
Future works may perform the hardware validation of the method, including noise on the spacecraft's state measurements and the reconstruction of the base velocity. Moreover, they may also validate the isolation strategy on hardware.

APPENDIX

A. Derivation of the relations (17)

In this section, the mathematical derivation of the relations (17) is reported.
Deriving the relations (17a) and (17b) is straightforward. Indeed, the differentiation of the momenta $\boldsymbol{h}_c^t$ and $\boldsymbol{h}_c^r$, which are expressed in frame $\mathcal{C}$, rotating with an angular velocity $\boldsymbol{\omega}_b$, results in

$$\dot{\boldsymbol{h}}_c^t + [\boldsymbol{\omega}_b]^\wedge \boldsymbol{h}_c^t = \boldsymbol{f}_{c,tot} \tag{40}$$

$$\dot{\boldsymbol{h}}_c^r + [\boldsymbol{\omega}_b]^\wedge \boldsymbol{h}_c^r = \boldsymbol{m}_{c,tot} \tag{41}$$

where $\boldsymbol{f}_{c,tot} \in \mathbb{R}^3$, $\boldsymbol{m}_{c,tot} \in \mathbb{R}^3$ are the total centroidal force and moment acting on the system. Recalling that $\boldsymbol{h}_c^t = m\boldsymbol{v}_c$ and comparing Eq. (40) with the first row of Eq. (15), the first relation (17a) is obtained. Similarly, comparing Eq. (41) with the second row of Eq. (15), the second relation (17b) is obtained.
For what concerns the third relation (17c), a quasi-Lagrangian approach [28] is used to rederive the joint equation in (15). Then, the relation (17c) is obtained by comparison of the quasi-Lagrangian joint dynamics formulation with the third row of Eq. (15). In the quasi-Lagrangian formulation, the generalized velocities $\boldsymbol{v}_c$ and $\boldsymbol{h}_c^r$ are called quasi-velocities since they are not integrable. In order to derive the dynamic equations, some integrable generalized coordinates $\boldsymbol{y} \in \mathbb{R}^{6+n}$ are defined, whose derivatives are related to the quasi-velocities as follows:

$$\begin{bmatrix} \boldsymbol{v}_c \\ \boldsymbol{h}_c^r \\ \dot{\boldsymbol{q}} \end{bmatrix} = \begin{bmatrix} \boldsymbol{E} & -[\boldsymbol{r}_c]^\wedge \boldsymbol{J}_\Phi^{-1} & \boldsymbol{0} \\ \boldsymbol{0} & \boldsymbol{I}_c \boldsymbol{J}_\Phi^{-1} & \boldsymbol{I}_c \bar{\boldsymbol{J}}_\omega \\ \boldsymbol{0} & \boldsymbol{0} & \boldsymbol{E} \end{bmatrix} \begin{bmatrix} \dot{\boldsymbol{r}}_c \\ \dot{\boldsymbol{\Phi}} \\ \dot{\boldsymbol{q}} \end{bmatrix} = \boldsymbol{\Xi}^T \dot{\boldsymbol{y}}, \tag{42}$$

where $\boldsymbol{r}_c \in \mathbb{R}^3$, $\dot{\boldsymbol{r}}_c \in \mathbb{R}^3$ are the position of the CM of the whole system expressed in $\mathcal{C}$ and its time derivative, respectively; $\boldsymbol{\Phi} \in \mathbb{R}^3$, $\dot{\boldsymbol{\Phi}} \in \mathbb{R}^3$ are the Euler angle vector and its time derivative, respectively; $\boldsymbol{J}_\Phi \in \mathbb{R}^{3\times 3}$ is the Jacobian mapping $\boldsymbol{\omega}_b$ in $\dot{\boldsymbol{\Phi}}$. The matrix $\boldsymbol{\Xi}$ is function of the generalized coordinates $\boldsymbol{y}$. Note that any rotation parameterization different from the Euler angles can be used without affecting the following joints dynamics derivation.
Introducing $\boldsymbol{x} = [\boldsymbol{v}_c^T \ \boldsymbol{h}_c^{rT} \ \dot{\boldsymbol{q}}^T]^T \in \mathbb{R}^{6+n}$ and assuming that $\boldsymbol{\Xi}^T$ is invertible, the following relation can be written:

$$\dot{\boldsymbol{y}} = \boldsymbol{\Omega}\boldsymbol{x} \tag{43}$$

where $\boldsymbol{\Omega} = \boldsymbol{\Xi}^{-T} \in \mathbb{R}^{(6+n)\times(6+n)}$.
Exploiting Eqs. (42)-(43), the quasi-Lagrangian formulation can be derived from the standard one [28], resulting in

$$\delta \boldsymbol{y}^T \left(\boldsymbol{\Xi} \frac{d}{dt} \left[\frac{\partial T}{\partial \boldsymbol{x}} \right] + \dot{\boldsymbol{\Xi}} \frac{\partial T}{\partial \boldsymbol{x}} - \frac{\partial T}{\partial \boldsymbol{y}} - \boldsymbol{H} \frac{\partial T}{\partial \boldsymbol{x}} - \boldsymbol{Q} \right) = 0, \tag{44}$$

where

$$\boldsymbol{H} = \begin{bmatrix} \boldsymbol{x}^T \boldsymbol{\Omega}^T \frac{\partial \boldsymbol{\Xi}}{\partial y_1} \\ \vdots \\ \boldsymbol{x}^T \boldsymbol{\Omega}^T \frac{\partial \boldsymbol{\Xi}}{\partial y_{6+n}} \end{bmatrix} \in \mathbb{R}^{(6+n)\times(6+n)}; \tag{45}$$

$\boldsymbol{Q} \in \mathbb{R}^{6+n}$ is the vector of the generalized forces; $T \in \mathbb{R}$ is the kinetic energy of the system expressed in terms of $\boldsymbol{x}$. The potential energy is assumed to be zero. T can be computed as follows

$$T = \frac{1}{2} \left(m \boldsymbol{v}_c^T \boldsymbol{v}_c + \dot{\boldsymbol{q}}^T \boldsymbol{M}_m^* \dot{\boldsymbol{q}} + \boldsymbol{h}_c^{rT} \boldsymbol{I}_c^{-T} \boldsymbol{h}_c^r \right). \tag{46}$$

The matrices $\dot{\boldsymbol{\Xi}}$ and $\boldsymbol{\Omega}^T \frac{\partial \boldsymbol{\Xi}}{\partial y_i}$, appearing in Eqs. (44)-(45), can be expanded as

$$\dot{\boldsymbol{\Xi}} = \begin{bmatrix} \boldsymbol{0} & \boldsymbol{0} & \boldsymbol{0} \\ \dot{\boldsymbol{J}}_\Phi^{-T} [\boldsymbol{r}_c]^\wedge + \boldsymbol{J}_\Phi^{-T} [\dot{\boldsymbol{r}}_c]^\wedge & \dot{\boldsymbol{J}}_\Phi^{-T} \boldsymbol{I}_c^T + \boldsymbol{J}_\Phi^{-T} \dot{\boldsymbol{I}}_c^T & \boldsymbol{0} \\ \boldsymbol{0} & \dot{\bar{\boldsymbol{J}}}_\omega^T \boldsymbol{I}_c^T + \bar{\boldsymbol{J}}_\omega^T \dot{\boldsymbol{I}}_c^T & \boldsymbol{0} \end{bmatrix} \tag{47}$$

$$\boldsymbol{\Omega}^T \frac{\partial \boldsymbol{\Xi}}{\partial y_i} = \begin{bmatrix} \boldsymbol{0} & \boldsymbol{0} & \boldsymbol{0} \\ \boldsymbol{I}_c^{-T} \boldsymbol{J}_\Phi^T \frac{\partial (\boldsymbol{J}_\Phi^{-T} [\boldsymbol{r}_c]^\wedge)}{\partial y_i} & \boldsymbol{I}_c^{-T} \boldsymbol{J}_\Phi^T \frac{\partial (\boldsymbol{J}_\Phi^{-T} \boldsymbol{I}_c^T)}{\partial y_i} & \boldsymbol{0} \\ -\bar{\boldsymbol{J}}_\omega^T \boldsymbol{J}_\Phi^T \frac{\partial (\boldsymbol{J}_\Phi^{-T} [\boldsymbol{r}_c]^\wedge)}{\partial y_i} & -\bar{\boldsymbol{J}}_\omega^T \boldsymbol{J}_\Phi^T \frac{\partial (\boldsymbol{J}_\Phi^{-T} \boldsymbol{I}_c^T)}{\partial y_i} + \frac{\partial (\bar{\boldsymbol{J}}_\omega^T \boldsymbol{I}_c^T)}{\partial y_i} & \boldsymbol{0} \end{bmatrix} \tag{48}$$

Therefore, the matrix $\boldsymbol{H}$ has this form:

$$\boldsymbol{H} = \begin{bmatrix} \boldsymbol{x}^T \boldsymbol{\Omega}^T \frac{\partial \boldsymbol{\Xi}}{\partial y_1} \\ \vdots \\ \boldsymbol{x}^T \boldsymbol{\Omega}^T \frac{\partial \boldsymbol{\Xi}}{\partial y_{6+n}} \end{bmatrix} = \begin{bmatrix} \boldsymbol{H}_t & \boldsymbol{H}_{tr} & \boldsymbol{0} \\ \boldsymbol{H}_{rt} & \boldsymbol{H}_r & \boldsymbol{0} \\ \boldsymbol{H}_{mt} & \boldsymbol{H}_{mr} & \boldsymbol{0} \end{bmatrix} \tag{49}$$

Since the joints dynamics is of interest, only the last n rows of the Lagrangian system can be considered. Hence, only the last n rows of $\boldsymbol{H}$ are expanded. It can be noted that $\boldsymbol{H}_{mt} = \boldsymbol{0}$ because neither $\boldsymbol{J}_\Phi$ nor $\boldsymbol{r}_c$ depends on $\boldsymbol{q}$, while $\boldsymbol{H}_{mr}$ can be expanded as follows

$$\begin{aligned} \boldsymbol{H}_{mr} &= \begin{bmatrix} \boldsymbol{h}_c^{rT} \boldsymbol{I}_c^{-T} \frac{\partial \boldsymbol{I}_c^T}{\partial q_1} + \dot{\boldsymbol{q}}^T \frac{\partial \bar{\boldsymbol{J}}_\omega^T}{\partial q_1} \boldsymbol{I}_c^T \\ \vdots \\ \boldsymbol{h}_c^{rT} \boldsymbol{I}_c^{-T} \frac{\partial \boldsymbol{I}_c^T}{\partial q_n} + \dot{\boldsymbol{q}}^T \frac{\partial \bar{\boldsymbol{J}}_\omega^T}{\partial q_n} \boldsymbol{I}_c^T \end{bmatrix} = \\ &= -\boldsymbol{I}_{c/q}^{-T} \boldsymbol{I}_c^T + \bar{\boldsymbol{J}}_{\omega/q}^T \boldsymbol{I}_c^T, \end{aligned} \tag{50}$$

where $\boldsymbol{I}_{c/q}^{-T}$, $\bar{\boldsymbol{J}}_{\omega/q}^T$ are reported in Eqs. (18), respectively.
Considering that

$$\frac{\partial T}{\partial \boldsymbol{x}} = \begin{bmatrix} m \boldsymbol{v}_c \\ \boldsymbol{I}_c^{-T} \boldsymbol{h}_c^r \\ \boldsymbol{M}_m^* \dot{\boldsymbol{q}} \end{bmatrix}, \qquad \frac{\partial T}{\partial \boldsymbol{y}} = \boldsymbol{0}, \tag{51}$$

after some simplification, the joints dynamic equation turns out to be

$$\begin{aligned} \bar{\boldsymbol{J}}_\omega^T \boldsymbol{I}_c^T (\boldsymbol{I}_c^{-T} \dot{\boldsymbol{h}}_c^r + \dot{\boldsymbol{I}}_c^{-T} \boldsymbol{h}_c^r) + \boldsymbol{M}_m^* \ddot{\boldsymbol{q}} + \dot{\boldsymbol{M}}_m^* \dot{\boldsymbol{q}} + \dot{\bar{\boldsymbol{J}}}_\omega^T \boldsymbol{h}_c^r - \frac{1}{2} (\boldsymbol{M}_{m/q}^* \dot{\boldsymbol{q}} - \boldsymbol{I}_{c/q}^{-T} \boldsymbol{h}_c^r) - \bar{\boldsymbol{J}}_{\omega/q}^T \boldsymbol{h}_c^r + \\ + \bar{\boldsymbol{J}}_\omega^T \dot{\boldsymbol{I}}_c^T \boldsymbol{I}_c^{-T} \boldsymbol{h}_c^r = \boldsymbol{\tau}_{tot} - \bar{\boldsymbol{J}}_v^T \boldsymbol{f}_{b,tot} \end{aligned} \tag{52}$$

where $\boldsymbol{\tau}_{tot} \in \mathbb{R}^n$ are the total torques acting on the joints, i.e., including commanded torques and disturbance torques; $\boldsymbol{f}_{b,tot} \in \mathbb{R}^n$ are the total forces acting on the base, i.e., including commanded forces and disturbance forces.
Substituting $\dot{\boldsymbol{h}}_c^r$ from Eq. (41) and $\dot{\boldsymbol{I}}_c^T = -\boldsymbol{I}_c^T \dot{\boldsymbol{I}}_c^{-T} \boldsymbol{I}_c^T$, and using relations (13) and (14), the dynamics (52) can be rewritten as

$$\boldsymbol{M}_m^* \ddot{\boldsymbol{q}} + (\dot{\boldsymbol{M}}_m^* - \frac{1}{2}\boldsymbol{M}_{m/q}^*)\dot{\boldsymbol{q}} + (\dot{\bar{\boldsymbol{J}}}_\omega^T - \bar{\boldsymbol{J}}_\omega^T [\boldsymbol{\omega}_b]^\wedge + \frac{1}{2}\boldsymbol{I}_{c/q}^{-T} - \bar{\boldsymbol{J}}_{\omega/q}^T)\boldsymbol{h}_c^r = \bar{\boldsymbol{\tau}}_{tot}, \tag{53}$$

where $\bar{\boldsymbol{\tau}}_{tot} = \bar{\boldsymbol{\tau}} + \bar{\boldsymbol{\tau}}_{ext} \in \mathbb{R}^n$.
Finally, comparing Eq. (53) and the third row of Eq. (15), the relation (17c) can be obtained.

B. A note on the computation of the partial derivatives in Eqs. (18)

The matrix $\boldsymbol{I}_c$ can be written using the inertia model (2) as it has been done for $\bar{\boldsymbol{J}}_\omega$ and $\boldsymbol{M}_m^*$ in Eqs. (11) and (16), respectively, and it results in

$$\boldsymbol{I}_c = \boldsymbol{M}_r - \frac{1}{m}\boldsymbol{M}_{tr}^T \boldsymbol{M}_{tr}. \tag{54}$$

Therefore, the partial derivatives of $\boldsymbol{I}_c^{-T}$, $\bar{\boldsymbol{J}}_\omega^T$ and $\boldsymbol{M}_m^*$ with respect to $\boldsymbol{q}$, required in the Eqs. (18), can be easily computed knowing the partial derivative with respect to $\boldsymbol{q}$ of the inertia matrix $\boldsymbol{M}$ in Eq. (2). To this aim, an efficient algorithm, that can run in real-time, has been proposed in [29] and used here in both simulative and hardware validation of the proposed observer.

Conflict of interest

The authors have no conflict of interest to declare.

References

[1] B. Siciliano, O. Khatib, Springer handbook of robotics, Springer, 2016.

[2] K. Yoshida, N. Sashida, R. Kurazume, Y. Umetani, Modeling of collision dynamics for space free-floating links with extended generalized inertia tensor, in: Robotics and Automation, 1992. Proceedings., 1992 IEEE International Conference on, IEEE, 1992, pp. 899–904.

[3] X. Cyril, G. J. Jaar, A. K. Misra, The effect of payload impact on the dynamics of a space robot, in: Intelligent Robots and Systems' 93, IROS'93. Proceedings of the 1993 IEEE/RSJ International Conference on, Vol. 3, IEEE, 1993, pp. 2070–2075.

[4] L.-B. Wee, M. W. Walker, On the dynamics of contact between space robots and configuration control for impact minimization, IEEE Transactions on Robotics and Automation 9 (5) (1993) 581–591.

[5] D. N. Nenchev, K. Yoshida, Impact analysis and post-impact motion control issues of a free-floating space robot subject to a force impulse, IEEE Transactions on Robotics and Automation 15 (3) (1999) 548–557.

[6] S. A. A. Moosavian, E. Papadopoulos, On the control of space free-flyers using multiple impedance control, in: Robotics and Automation, 1997. Proceedings., 1997 IEEE International Conference on, Vol. 1, IEEE, 1997, pp. 853–858.

[7] H. Nakanishi, K. Yoshida, Impedance control for free-flying space robots-basic equations and applications, in: 2006 IEEE/RSJ International Conference on Intelligent Robots and Systems, IEEE, 2006, pp. 3137–3142.

[8] K. Yoshida, D. Dimitrov, H. Nakanishi, On the capture of tumbling satellite by a space robot, in: Intelligent robots and systems, 2006 IEEE/RSJ international conference on, IEEE, 2006, pp. 4127–4132.

[9] K. Yoshida, H. Nakanishi, H. Ueno, N. Inaba, T. Nishimaki, M. Oda, Dynamics, control and impedance matching for robotic capture of a non-cooperative satellite, Advanced Robotics 18 (2) (2004) 175–198.

[10] A. M. Giordano, G. Garofalo, A. Albu-Schaffer, Momentum dumping for space robots, in: Decision and Control (CDC), 2017 IEEE 56th Annual Conference on, IEEE, 2017, pp. 5243–5248.

[11] A. Flores-Abad, M. Nandayapa, M. A. Garcia-Teran, Force sensorless impedance control for a space robot to capture a satellite for on-orbit servicing, in: 2018 IEEE Aerospace Conference, IEEE, 2018.

[12] A. De Luca, A. Albu-Schaffer, S. Haddadin, G. Hirzinger, Collision detection and safe reaction with the dlr-iii lightweight manipulator arm, in: 2006 IEEE/RSJ International Conference on Intelligent Robots and Systems, IEEE, 2006, pp. 1623–1630.

[13] S. Haddadin, A. De Luca, A. Albu-Schäffer, Robot collisions: A survey on detection, isolation, and identification, IEEE Transactions on Robotics 33 (6) (2017) 1292–1312.

[14] T. Ren, Y. Dong, D. Wu, K. Chen, Collision detection and identification for robot manipulators based on extended state observer, Control Engineering Practice 79 (2018) 144–153.

[15] F. Flacco, A. Paolillo, A. Kheddar, Residual-based contacts estimation for humanoid robots, in: Humanoid Robots (Humanoids), 2016 IEEE-RAS 16th International Conference on, IEEE, 2016, pp. 409–415.

[16] J. Vorndamme, M. Schappler, S. Haddadin, Collision detection, isolation and identification for humanoids, in: 2017 IEEE International Conference on Robotics and Automation (ICRA), IEEE, 2017, pp. 4754–4761.

[17] T. Tomić, C. Ott, S. Haddadin, External wrench estimation, collision detection, and reflex reaction for flying robots, IEEE Transactions on Robotics 33 (6) (2017) 1467–1482.

[18] J. Artigas, M. De Stefano, W. Rackl, R. Lampariello, B. Brunner, W. Bertleff, R. Burger, O. Porges, A. Giordano, C. Borst, et al., The oos-sim: An on-ground simulation facility for on-orbit servicing robotic operations, in: 2015 IEEE International Conference on Robotics and Automation (ICRA), IEEE, 2015, pp. 2854–2860.

[19] F. Cavenago, A. M. Giordano, M. Massari, Contact force observer for space robots, in: 2019 IEEE 58th Conference on Decision and Control (CDC), IEEE, 2019, pp. 2528–2535.

[20] R. M. Murray, A mathematical introduction to robotic manipulation, CRC press, 2017.

[21] A. M. Giordano, D. Calzolari, A. Albu-Schäffer, Workspace fixation for free-floating space robot operations, in: Robotics and Automation (ICRA), 2018 IEEE International Conference on, IEEE, 2018.

[22] J. L. Crassidis, F. L. Markley, Unscented filtering for spacecraft attitude estimation, Journal of guidance, control, and dynamics 26 (4) (2003) 536–542.

[23] J. L. Crassidis, Sigma-point kalman filtering for integrated gps and inertial navigation, IEEE Transactions on Aerospace and Electronic Systems 42 (2) (2006) 750–756.

[24] J. Gil-Fernández, T. Prieto-Llanos, R. Panzeca, R. Drai, Autonomous gnc algorithms for neo impactor missions, in: Proceedings of the 20th International Symposium on Space Flight Dynamics, 2007, pp. 1–14.

[25] F. Cavenago, P. Di Lizia, M. Massari, A. Wittig, On-board spacecraft relative pose estimation with high-order extended kalman filter, Acta Astronautica 158 (2019) 55–67.

[26] F. Aghili, K. Parsa, Adaptive motion estimation of a tumbling satellite using laser-vision data with unknown noise characteristics, in: 2007 IEEE/RSJ International Conference on Intelligent Robots and Systems, IEEE, 2007, pp. 839–846.

[27] A. M. Giordano, C. Ott, A. Albu-Schäffer, Coordinated control of spacecraft's attitude and end-effector for space robots, IEEE Robotics and Automation Letters 4 (2) (2019) 2108–2115.

[28] J. M. Cameron, W. J. Book, Modeling mechanisms with nonholonomic joints using the Boltzmann-Hamel equations, The International Journal of Robotics Research 16 (1) (1997) 47–59.

[29] G. Garofalo, C. Ott, A. Albu-Schäffer, On the closed form computation of the dynamic matrices and their differentiations, in: 2013 IEEE/RSJ International Conference on Intelligent Robots and Systems, IEEE, 2013, pp. 2364–2359.